10-2022

Improving Moisture Content Estimation from Field Resistivity Measurements with Subsurface Structure Information

Hang Chen
Boise State University

Qifei Niu
Boise State University

Improving Moisture Content Estimation from Field Resistivity Measurements with Subsurface Structure Information

Hang Chen
Department of Geosciences
Boise State University
Boise, Idaho, USA

Qifei Niu*
Department of Geosciences
Boise State University
Boise, Idaho, USA
qifeiniu@boisestate.edu

Abstract

In Earth sciences, the measurement of soil and rock moisture content is essential in improving our understanding of various hydrologic processes. Recently, the electrical resistivity method has been frequently used to estimate the moisture content in the field. The uncertainty associated with resistivity-estimated moisture content is mainly from two sources: regularized inversion and petrophysical interpretation. In this study, to reduce the uncertainty, we propose (1) to use subsurface structural information from seismic refraction measurements to relax the smoothness-based regularization at structural boundaries and (2) to use structural unit-specific petrophysical relationships to translate resistivity into moisture content. The proposed methods are tested on a synthetic subsurface model featuring three distinct layers of a granitic critical zone (CZ). The results of the synthetic example show that both the spatial pattern and the moisture content values estimated with the new method are very close to the true model with low uncertainty. Compared to the traditional method, the estimation is significantly improved, particularly at the CZ boundaries, such as the regolith-fractured bedrock interface. We also apply the new method to a granitic hillslope to estimate the moisture content distribution from field resistivity measurements. Although no ground truth is available for validation, the estimated moisture content distributions exhibit some typical hydrological features in hillslopes, such as the perched water at the soil/rock interface and preferential flow path in fractured rocks. Therefore, it is concluded that incorporating structural information in resistivity inversion and using structural unit-specific petrophysical models can improve moisture content estimation from field resistivity measurements.

Keywords: moisture content, electrical resistivity, Monte Carlo, constrained inversion, subsurface structure

1. Introduction

In the shallow subsurface, weathering of bedrock results in a physically mobile, granular surface mantle that lacks relict rock structure (Pope, 2015), usually termed as soil (or regolith). The soil layer plays a critical role in the terrestrial water cycles by influencing the partitioning of precipitation between soil moisture, evaporation/evapotranspiration, deep infiltration (contributing to groundwater recharge), and runoff (Brooks et al., 2015). With advances in measurement techniques (e.g., Robinson et al., 2008), soil moisture has become a regular state variable in many hydrologic, ecologic, and climate models (Dorigo et al., 2011). Recently, it has been realized that the fractured bedrock beneath the soil (or regolith) layer also influences groundwater recharge, evapotranspiration, base flow, and stream water chemistry (e.g., Rempe and Dietrich, 2018). Thus, many efforts have been made to incorporate rock moisture as a state variable into hydrologic, ecological, and climate models (e.g., Ackerer et al., 2021). In this regard, soil and rock moisture measurements are essential in improving our understanding of various hydrologic processes and our projections of Earth's water resources.

Soil moisture can be measured either with satellite remote sensing techniques (Mohanty et al., 2017) or in situ, for example, using soil moisture probes/sensors (Dobriyal et al., 2012). Remote sensing can cover a large region, and thus the measured soil moisture data are valuable for the calibration and verification of large-scale hydrologic modeling (Vischel et al., 2008; Sánchez et al., 2010). The primary limitation of satellite-based remote sensing is that the moisture data are only available for near-surface soils (~5 cm). In contrast, soil moisture probes/sensors (e.g., time-domain reflectometry) installed in soil pits can reach down to the bedrock and showed excellent vertical resolutions (e.g.,

Heimovaara and Bouten, 1990). If these moisture probes are distributed over large regions to form a soil moisture monitoring network (e.g., Benninga et al., 2018), the spatial-temporal soil moisture patterns can be revealed. The monitored soil moisture data can also be used for the calibration and verification of distributed hydrologic models. One limitation of this point-based soil moisture measurement is the limited support volume (~cm^3), which is inconsistent with the mesh volume used in most hydrologic models (from ~m^3 to ~ km^3).

Rock moisture measurement has been conducted in the field in many ecohydrological studies. The current practice is to measure in boreholes using non-destructive geophysical techniques, such as the neutron probe (Rempe and Dietrich, 2018; Hahm et al., 2020) and nuclear magnetic resonance (Schmidt and Rempe, 2020). The typical support volume of these borehole-based tools is ~m^3, and the instrument can be lowered down to ~10s m with a vertical resolution of ~25 cm (e.g., Hahm et al., 2020). Such rock moisture data are critical for understanding the role of fractured bedrock in regulating the ecohydrological partitioning at the land surface (Brooks et al., 2015). However, one primary drawback of the borehole-based rock moisture measurement is the high cost, which prohibits the establishment of a monitoring network for watershed- or catchment-scale applications. Given the limitations of existing soil and rock moisture measurement techniques, there is a need to develop cost-effective techniques that can measure soil and rock moisture content at an intermediate scale (from hillslope to catchment scale) with a high vertical resolution.

Near-surface geophysical methods have been frequently used in hydrological studies to provide spatio-temporal information on the subsurface, from sub-meter pedon scales to ~km watershed scales (Binley et al., 2015; Parsekian et al., 2015). Among them, the electrical resistivity method received considerable attention (e.g., Garré et al., 2011; Coscia et al., 2011) due to the strong influence of water content on the electrical resistivity of geological materials (Lesmes and Friedman, 2005). Many models have been developed to describe the relationship between resistivity and water content (Friedman, 2005; Laloy et al., 2011; Romero-Ruiz et al., 2022). In particular, many physics-based models are available, including the differential effective medium models (Sen et al., 1981), percolation theory-based models (Ghanbarian et al., 2014), and the bundle of capillary tubes models (Niu et al., 2015). Recently, significant advances have been made in almost all aspects of resistivity method, including instrumentation (Slater and Binley, 2021), inversion (Linde and Doetsch, 2016), and petrophysics (Day-Lewis et al, 2017). These advances have led to increased use of the resistivity method in estimating moisture content and monitoring hydrologic processes in field applications (e.g., Slater and Binley, 2021; Leopold et al., 2021).

It is also well known that the moisture content estimated from resistivity tomography may contain significant uncertainties mainly due to two factors (Linde et al., 2017). First, resistivity inversion is an ill-posed problem (Roy, 1962), and many "equally good" resistivity models exist to fit the measurements. To have a unique solution, regularizations are usually applied in the inversion (Zhdanov 2002) to force the optimal model to be close to some specified models or have a smooth variation (e.g., Vauhkonen et al., 1998). However, the applied regularizations may not be realistic for subsurfaces having contrasting properties or sharp boundaries (Zhou et al., 2014). Second, the relationships between resistivity and moisture content of geological materials are influenced by many material properties such as texture, mineralogy, and pore water chemistry. Due to subsurface heterogeneity, using one resistivity-moisture content relationship to interpret the entire subsurface tends to create significant errors (Tso et al., 2019). Sometimes, the interpreted moisture content could be erroneous and thus misleading for hydrological applications.

In the applied geophysics community, a number of methods have been developed the address the aforementioned problems. To resolve the problem related to regularization, many efforts have been devoted to stochastic inversions (e.g., Tso et al., 2021) and joint inversions (Linde and Doetsch, 2016). The most popular strategy in joint inversions is probably the use of the cross-gradient constraint (Doetsch et al., 2010; Gallardo and Meju, 2004), which assumes different physical properties (e.g., velocity and resistivity) have similar spatial patterns (i.e., structural similarity). The second type of method uses the structural information from one data set (e.g., travel time) to guide the inversion of a second geophysical data set (e.g., resistivity) by manipulating the regularization term in the inversion. Relevant approaches include image-guided inversion (e.g., Zhou et al., 2014) and regularization relaxation at structural boundaries (e.g., Slater and Binley. 2006; Johnson et al., 2012; Jiang et al., 2020). Using different resistivity models to estimate moisture content in heterogeneous subsurface is not very common (e.g., González et al., 2021; Pleasants et al., 2022), partially due to the difficulty in determining the actual structural boundaries. Alternatively, a number of studies account for spatial heterogeneity by quantifying the petrophysical uncertainty (Brunetti et al., 2017; Brunetti and Linde, 2018; Tso et al., 2019).

Recent advances in structure-based resistivity inversions have not been commonly used in moisture estimations with field resistivity measurements. Therefore, this study's objective is to test if the resistivity-estimated moisture content can be improved by incorporating structural information into the resistivity inversion and applying structural unit-specific resistivity models in the petrophysical interpretation. This proposed new approach would be particularly useful for structurally heterogeneous subsurfaces such as critical zone in mountainous regions. In this study, the structural information will be used in resistivity inversion to relax the smoothness-based regularization at structural boundaries in the subsurface (Doetsch et al., 2010). By doing this, we may keep the sharp resistivity contrasts across some structural boundaries (Zhou et al., 2014). The structural information of the subsurface can be from geological mapping (Wellmann et al., 2018), borehole logging data (Wisén et al., 2005), or other geophysical results (Zhou et al., 2014). We also use the structural information to perform zonation so that the structural unit-specific resistivity model can be applied to reduce the petrophysical uncertainties related to moisture estimations. In this study, the structure information of the subsurface will be obtained from seismic refraction tomography, which has been frequently used in practice to delineate the structural features of shallow subsurface (Flinchum et al., 2018a).

The paper is organized as follows. First, we introduce the theories of incorporating structural information into traditional resistivity inversions and conducting the subsequent moisture estimation. We then design a synthetic subsurface model for testing our proposed method. To quantify the petrophysical uncertainties related to moisture estimation, Monte Carlo simulations are carried out to consider the variability in model parameters of the resistivity-moisture content relationships. We also test our method using field data collected from a small catchment in western mountain regions of the US. Major conclusions are summarized at the end of the paper.

2. Theory

This section briefly describes the theoretical background of the proposed strategy of incorporating the structure information extracted from seismic surveys into resistivity inversions. We also introduce the new method for moisture estimation and uncertainty quantification using structural unit-specific petrophysical models (i.e., resistivity-moisture content relationships). The workflow of the proposed methods is shown in Figure 1, and detailed explanations are described as follows.

2.1. Smoothness-Constrained Resistivity Inversion

In electrical resistivity surveys, a pair of electrodes are usually used to inject electric current into the subsurface, and other electrodes are used to measure the induced electrical potential on the ground surface. This process is repeated at different locations with different combinations of electrodes. The measurements are usually presented as apparent resistivity data (Perrone et al., 2014). Forward modeling of electrical resistivity surveys involves solving the governing equation of electric current flow in heterogeneous materials under appropriate boundary conditions. In matrix format, the resistivity measurements (apparent resistivity data) **d** obtained from a resistivity survey can be expressed as (e.g., Pidlisecky and Knight, 2008)

$$\mathbf{d} = \mathbf{A}(\mathbf{m}) \tag{1}$$

where **m** is the model parameters defining the subsurface resistivity model, and **A** is the relevant forward operator.

To obtain a unique resistivity model **m** from **d**, regularized inversions are usually carried out. For example, the Tikhonov regularization (e.g., Zhdanov, 2002) is often used in resistivity inversion, and the object function $\Phi(\mathbf{m})$ can be expressed as the sum of two terms,

$$\Phi(\mathbf{m}) = \Phi_{\mathrm{d}}(\mathbf{m}) + \lambda\Phi_{\mathrm{m}}(\mathbf{m}) \tag{2}$$

where $\Phi_{\mathrm{d}}(\mathbf{m})$ quantifies the measurement or data misfit, $\Phi_{\mathrm{m}}(\mathbf{m})$ is the Tikhonov regularization term, and the parameter λ balances the data misfit and regularization. In practice, $\Phi_{\mathrm{d}}(\mathbf{m})$ is usually calculated as the *l2*-norm of the difference between the observed resistivity data $\mathbf{d}_{\mathrm{obs}}$ and theoretical responses **d(m)**, expressed as

$$\Phi_{\mathrm{d}}(\mathbf{m}) = \|\mathbf{W}_{\mathrm{d}}(\mathbf{d}(\mathbf{m}) - \mathbf{d}_{\mathrm{obs}})\|^2 \tag{3}$$

where $\mathbf{W}_{\mathrm{d}}$ is a weighting matrix and its elements are usually related to resistivity measurement errors. If the errors are assumed uncorrelated, $\mathbf{W}_{\mathrm{d}}$ will be a diagonal matrix, and each diagonal element can be chosen as the inverse of the associated measurement error. The regularization term $\Phi_{\mathrm{m}}(\mathbf{m})$ applies some constraints to the model **m** and can be written as (e.g., Jordi et al., 2018)

$$\Phi_{\mathrm{m}}(\mathbf{m}) = \|\mathbf{W}_{\mathrm{m}}^{\mathrm{s}}(\mathbf{m} - \mathbf{m}_{\mathrm{ref}})\|^2 \tag{4}$$

where $\mathbf{W}_{\mathrm{m}}^{\mathrm{s}}$ is the constraint matrix for $\mathbf{m}$ and $\mathbf{m}_{\mathrm{ref}}$ is a reference resistivity model, which may contain prior information on the resistivity of the subsurface (e.g., from borehole resistivity logging). The constraint matrix $\mathbf{W}_{\mathrm{m}}^{\mathrm{s}}$ is usually chosen as the first- or second-order gradient operator matrix, and thus it imposes a smoothness constraint to the resistivity model $\mathbf{m}$.

The optimal resistivity model can be obtained by minimizing the objective function $\Phi(\mathbf{m})$ in Equation (2). This study uses the Gauss-Newton method to determine the optimal resistivity model iteratively (Günther et al., 2006). At step k, the model update $\Delta\mathbf{m}^k$ to the current resistivity model $\mathbf{m}^k$ can be determined by solving the following equation (e.g., Jordi et al., 2018)

$$\begin{bmatrix}\mathbf{W}_{\mathrm{d}}\mathbf{J}^k \\ \lambda\mathbf{W}_{\mathrm{m}}^{\mathrm{s}}\end{bmatrix}\Delta\mathbf{m}^k = \begin{bmatrix}\mathbf{W}_{\mathrm{d}}(\mathbf{d}(\mathbf{m}^k) - \mathbf{d}_{\mathrm{obs}}) \\ \lambda\mathbf{W}_{\mathrm{m}}^{\mathrm{s}}(\mathbf{m}^k - \mathbf{m}_{\mathrm{ref}})\end{bmatrix} \tag{5}$$

where $\mathbf{J}^k$ is the Jacobian matrix associated with resistivity forward modeling at step k. Thus, the new resistivity model at step k+1 can be updated as $\mathbf{m}^{k+1} = \mathbf{m}^k + \alpha\Delta\mathbf{m}^k$ where α is a line search parameter that prevents overshooting (e.g., Günther et al., 2006). This iterative process can be terminated if the model update is negligible or the parameter $\chi^2 = \Phi_d/n_d$ (where n_{d} is the data length) is close to 1 (Günther et al., 2006).

2.2. Extraction of Structural Information

The structural information of the subsurface can be extracted from a variety of datasets, such as seismic images and ground-penetrating radar images (e.g., Zhou et al., 2014; Doetsch et al., 2012; de Pasquale and Linde, 2017; de Pasquale et al., 2019). In this study, we use seismic refraction tomography to delineate the structural features of the subsurface, and the results are then used to constrain the resistivity inversion. The results of seismic refraction tomography (i.e., seismic velocity) are very sensitive to geological materials' microstructure, such as grain-to-grain arrangement (e.g., Falcon-Suarez et al., 2020) and the presence of fractures (e.g., Han, 2008). Other factors, such as water saturation (particularly close to the saturation), may also affect the seismic velocity of geological materials (e.g., Pride, 2005; Pasquet et al., 2016). Nevertheless, seismic velocity has been proven effective and is commonly used in earth sciences to characterize the subsurface's structural features and conduct zonation (e.g., Befus et al., 2011).

Here, we argue seismic surveys contain more structural information than resistivity methods, and thus the extracted structures can be used to constrain the resistivity inversion. From a mathematical point of view, seismic methods (refraction or reflection) and ground-penetrating radar are based on solving the wave equations. As a result, the vertical resolution is proportional to the inverse of the wavelength, and the wave carries impedance information along its entire ray path (e.g., Constable, 2010). In contrast, the resistivity method is based on solving the Laplace equation, which is a reduced form of the diffusion equation considering a zero frequency. The Laplace equation describes the potential-field problem, and the intrinsic resolution becomes almost nonexistent (Constable, 2010). Thus, structural information contained in seismic results could be used to guide the resistivity inversion to reconstruct the subsurface resistivity distribution.

To extract the structural information, in this study, we first invert the first arrival time data to construct the subsurface velocity model. In the inversion, theoretical travel times can be calculated using conventional ray-tracing methods such as shooting (e.g., White, 1989) and bending (Wesson, 1971); the velocity model can be updated using the Gauss-Newton method iteratively. Similarly, regularization is imposed to ensure a unique solution. Here, we use an anisotropic smooth matrix, which applies different weights to vertical and horizontal directions to improve the vertical resolution (e.g., Jiang et al., 2020; Wagner and Uhlemann, 2021). It should be addressed that, in seismic inversion, the regularization mainly influences the inverted velocity values, and its influence on the structural features of the velocity model is minor (e.g., Zhang and Toksöz, 1998; Jiang and Zhang, 2017). That said, the structural information (e.g., the boundary of structural units) extracted from the inverted velocity model is not significantly affected by the selection of regularization schemes (e.g., Van Avendonk et al., 2004).

The current practice of determining the subsurface structures from a velocity model is to pick up representative velocity values as the boundaries between different structural units (e.g., St Clair et al., 2015; Flinchum et al., 2018b). This method may introduce significant biases as the inverted velocity values may be influenced by the selected regularization scheme. In this study, we propose a new method, and we demonstrate it using the velocity data collected

from a typical critical zone (CZ) site (Flinchum et al., 2022). As shown in Figure 2, we identify the three CZ layers (regolith, fractured bedrock, and fresh bedrock) from the velocity-depth profile by selecting segments featuring a relatively constant velocity gradient (red dash lines in Figure 2). Using the gradient rather than the absolute value of the velocity to distinguish CZ layers is supported by the distinct velocity-porosity relationships observed in different CZ materials (see Figure 3). In fractured bedrock, it is the fracture density that controls the velocity (e.g., Boadu and Long, 1996; Boadu, 1998); in contrast, the velocity of granular material (e.g., in regolith) is mainly controlled by the grain-to-grain contact (i.e., fabric). Therefore, the velocity-porosity curve of fractured rocks is much steeper than that of granular materials [see Figure 3 or empirical equations in Zhukov and Kuzmin (2020)]. Assuming a simple linear relationship between porosity and depth (e.g., see experimental data in Holbrook et al., 2019), it is easy to understand that the velocity gradient should differ noticeably in regolith and fractured bedrocks (e.g., see Figure 2).

2.3. Structure Constrained Resistivity Inversion

Once the structure information is extracted from the velocity image, it will be used to constrain the resistivity inversion. In this study, we follow the method used by Rücker (2010) and Jiang et al. (2020) to incorporate structural information in resistivity inversion. The regularization-imposed smoothness constraint at boundaries between different structural units can then be removed. Mathematically, the structural information will be added to the constraint matrix $\mathbf{W}_{\mathrm{m}}^{\mathrm{s}}$ to affect the resistivity model $\mathbf{m}$. Thus, the matrix $\mathbf{W}_{\mathrm{m}}^{\mathrm{s}}$ is changed to a new matrix $\mathbf{W}_{\mathrm{m}}^{\mathrm{c}}$ having the following form (Jiang et al., 2020),

$$\mathbf{W}_{\mathrm{m}}^{\mathrm{c}} = \mathbf{W}_{\mathrm{c}}\mathbf{W}_{\mathrm{m}}^{\mathrm{s}} \tag{6}$$

where the matrix $\mathbf{W}_{\mathrm{c}}$ is a diagonal matrix, and its elements are 1 for locations within a structural unit but 0 at structural boundaries (Jiang et al., 2020). Compared to smoothness-based regularization, this relaxed regularization can improve geophysical inversion results, particularly at the structural boundaries (Jiang et al., 2020; Skibbe et al., 2021).

2.4. Estimation of Moisture Content and Relevant Uncertainty

The reconstructed resistivity image can be translated into moisture content using resistivity-moisture content models (e.g., Lesmes and Friedman, 2005). In this study, it is proposed to take advantage of the existing petrophysical understanding of CZ materials. More specifically, we will treat different CZ layers as different materials, and thus each CZ layer (i.e., structural unit) will have its own resistivity-moisture content relationship. Note that the traditional method usually applies a single resistivity-moisture content relationship to the entire subsurface. Such a simple petrophysical interpretation could induce large uncertainty in the estimated moisture content due to subsurface heterogeneity (Tso et al., 2019). In contrast, we use structural unit-specific resistivity-moisture content relationships, which can account for, to a certain degree, the difference in material texture and mineralogy in different structural units. The uncertainty related to the estimated moisture content can be reduced if compared to the traditional method.

Here we use the Waxman and Smits (WS) model (Waxman and Smits, 1968; Doussan and Ruy, 2009) to link the electrical conductivity σ of geological materials to their volumetric moisture content θ, expressed as

$$\sigma = \frac{S^n}{F}\left(\sigma_{\mathrm{w}} + \frac{\sigma_{\mathrm{s}}}{S}\right) \tag{7}$$

where σ_{w} is the pore water conductivity, S is the water saturation ($S = \theta/\phi$ where ϕ is porosity), F is the formation factor ($F = \phi^{-m}$ where m is the porosity exponent or commonly known as cementation exponent), n is the saturation exponent, and σ_{s} is the surface conductivity associated with counter ions of the electrical double layer (Revil and Golver, 1998). Rearranging Equation 7 yields an implicit expression for θ,

$$\sigma = \sigma_{\mathrm{sat}}^{\mathrm{p}}\left(\frac{\theta}{\phi}\right)^n + \sigma_{\mathrm{sat}}^{\mathrm{s}}\left(\frac{\theta}{\phi}\right)^{n-1} \tag{8}$$

where $\sigma_{\mathrm{sat}}^{\mathrm{p}}=\sigma_{\mathrm{w}}/F$ is the conductivity of the soil at saturation contributed by the pore water and $\sigma_{\mathrm{sat}}^{\mathrm{s}}=\sigma_{\mathrm{s}}/F$ is the conductivity of the soil at saturation contributed from the counter ions of the electrical double layer. The sum of $\sigma_{\mathrm{sat}}^{\mathrm{p}}$ and $\sigma_{\mathrm{sat}}^{\mathrm{s}}$ is the saturated soil conductivity σ_{sat}. In practice, n, $\sigma_{\mathrm{sat}}^{\mathrm{p}}$, and $\sigma_{\mathrm{sat}}^{\mathrm{s}}$ can be determined by fitting Equation 8 to resistivity measurements of materials at variably saturated conditions. The saturation exponent n is related to the pore water connectivity or connectedness (e.g., Glover 2017). For unconsolidated materials, n ranges between 1.3 and 2 (e.g., Schön, 2015); for fractured rocks, n may be much smaller due to the well-connected fractures.

Even within a structural unit, the parameters of Equation 8 may still vary for materials at different locations. Using Equation 8 with a fixed set of parameters can still induce uncertainty in moisture estimation. To quantify this uncertainty, we conduct an uncertainty propagation analysis (e.g., Aster et al. 2005) using the Monte Carlo (MC) simulation. In the MC analysis, the parameters of the WS model in Equation 8 will be given a range rather than a single value. Since in the field electrical resistivity is more often used than electrical conductivity, in this study, we will use the saturated resistivity $\rho_{\mathrm{sat}} = 1/\sigma_{\mathrm{sat}} = 1/(\sigma_{\mathrm{sat}}^{\mathrm{p}} + \sigma_{\mathrm{sat}}^{\mathrm{s}})$ and saturated resistivity related to surface conduction $\rho_{\mathrm{sat}}^{\mathrm{s}} = 1/\sigma_{\mathrm{sat}}^{\mathrm{s}}$ to conduct the MC analysis. Thus, for each structural unit, we will have four petrophysical parameters (i.e., n, ϕ, ρ_{sat} and $\rho_{\mathrm{sat}}^{\mathrm{s}}$) to estimate the moisture content. For a typical CZ having three layers (regolith, fractured bedrock, and fresh bedrock), we then need 12 parameters. Among them, ρ_{sat} accounts for the combined influence of formation factor F (and thus porosity) and pore fluid conductivity, and $\rho_{\mathrm{sat}}^{\mathrm{s}}$ accounts for the combined influence of F and surface conductivity.

The parameters are randomly drawn from their plausible ranges and are used to convert resistivity into moisture content. With many realizations, we then can evaluate the possible range for the moisture content. It should be addressed that this MC-based uncertainty analysis only accounts for the petrophysical uncertainty. The uncertainty induced by resistivity inversion may also be quantified, for example, using the stochastic inversion method (e.g., Linde et al., 2017; de Pasquale et al. 2017; de Pasquale et al., 2019) or the method used in Tso et al., (2019).

3. Synthetic Example

In this section, we use a synthetic subsurface model to demonstrate the use of our proposed method for moisture content estimation and uncertainty analysis. The estimated moisture content is compared to the true values and the results of the traditional method to show the effectiveness of the new method.

3.1. Synthetic Subsurface Model

As shown in Figure 4a, we design a CZ model extending from the stream valley to the ridge with an average slope of ~16%. This CZ model is typical for mountain regions with granitic bedrock (e.g., Olona et al., 2010), and the subsurface under the hillslope consists of three layers: regolith, fractured rock, and fresh bedrock. The regolith layer is composed of unconsolidated materials weathered from the bedrock. In the model (Figure 4a), the thickness of regolith is ~0.5 m in the valley and increases gradually to ~4.0 m under the ridge. Fractures in the bedrock commonly form as a result of local/regional tectonic stresses or frost-cracking, and in this model, the depth of the fractured bedrock layer is ~0.5 m in the valley and increases to ~ 5.5 m under the ridge.

The ranges of the physical properties of the synthetic model are summarized in Table 1. Here, we assume these properties (ρ_{sat}, ϕ, $\rho_{\mathrm{sat}}^{\mathrm{s}}$ and n) are different for each CZ layer. In each CZ layer, these properties are also depth-dependent and spatially correlated (e.g., Western et al., 2004). For example, the regolith and fractured bedrock have a mean saturated resistivity of 900 Ω m and 1500 Ω m, respectively, to reflect the fact that the pore space in fractured rocks is generally smaller than that in the regolith. Regarding the spatial variability of ρ_{sat} and ϕ, we treat them as stationary random functions with uniform probability densities and autocovariance functions (e.g., Zhang et al., 2003; Chen and Niu, 2021), which are modeled with an exponential covariance model with two correlation lengths (vertical and horizontal directions). In the synthetic model, the horizontal and vertical correlation lengths are 20 m and 2 m, respectively, and the logarithmic variance of ρ_{sat} and ϕ are 0.2 and 0.1, respectively. Only the regolith layer considers the surface conductivity.

We assume the degree of saturation S in the model increases linearly with depth from S = 50% at the ground surface to fully saturation (S = 100%) at the fresh bedrock. Thus, we can generate a heterogeneous moisture content map, as shown in Figure 4b. Similar to field conditions (Flinchum et al., 2019), the moisture content in Figure 4b is generally high near the ground surface and low in the bedrock. Using Equation 9 and parameters in Table 1, we also calculate the resistivity distribution for the synthetic model, shown in Figure 4c. To generate the velocity model, we follow the method used in Flinchum et al. (2018b). For regolith, we used a velocity model based on Hertz–Mindlin contact theory and modified Hashin Shtrikman bounds (Mavko et al., 2020), and the effective fluid model (Mavko et al., 2020) and Gassmann's fluid substitution equation (Mavko et al., 2020) are used to calculate the velocity at various water saturations (e.g., Pasquet et al. 2016; Flinchum et al., 2018b). The differential effective medium model (e.g., Berryman, 1992) for the fractured and fresh bedrock, and the results are shown in Figure 4d. It is noted that these two theoretical models are used only for the purpose of generating realistic velocity values for different materials, and other models may also be used.

Synthetic seismic refraction and electrical resistivity tests are simulated on the subsurface model. In the modeling, 90 geophones and electrodes are collocated on the ground surface with a spacing of 1 m. In the seismic refraction test, 16 seismic sources are created on the ground surface with ~ 5 m spacing, and the travel time of the waves from the source to each geophone is calculated by solving the eikonal equation (e.g., Gallardo and Meju, 2004). In the resistivity survey, the Wenner array is used, and the electrode spacing ranges between 1 m and 30 m. We used the software package *PyGIMLi (https://www.pygimli.org/)* developed by Rücker et al. (2017) to simulate both seismic and resistivity tests, and in total, we collected 1424 travel-time and 1305 resistivity measurements. The travel time and apparent resistivity data are corrupted with 1% normally distributed random noises to account for measurement errors.

3.2. Seismic Results

The travel time data are inverted to reconstruct the velocity distribution of the synthetic model. During the inversion, 1% of the observed travel times are used as the diagonal elements in the matrix $\mathbf{W}_d$, and λ are 50 and 10 for the horizontal and vertical directions, respectively. In the inversion, the model was discretized into ~3200 cells, and the reconstructed velocity distribution is shown in Figure 5a. In general, the reconstructed velocity is quite similar to the true velocity distribution (Figure 4d), and the normalized root mean square deviation between the true and inverted velocity is only ~10%. In addition, the boundary between fresh bedrock and fractured bedrock is clearly identified in Figure 5a. The regolith-fractured bedrock interface may also be located (Figure 5a), although it is less obvious than the fresh bedrock-fractured bedrock interface.

A vertical transect is taken from the velocity model in Figure 5a at a distance x = 68 m, and the velocity-elevation profile is plotted in Figure 5b. We use the approach proposed in section 2.2 to determine the structural boundary between regolith, fractured rock, and fresh bedrock. As shown in Figure 5b, the velocity gradient in regions near the ground surface (e.g., elevation z > 35 m) is very small and increases to large values in the middle part of the profile (30 m < z < 35m). We use linear lines to fit the velocity-elevation curves in these two regions (top two red dash lines in Figure 5b), and the regolith-fractured rock interface can then be determined (e.g., z = 36 m in Figure 5b). Similarly, the boundary between the fractured and fresh bedrocks is determined as z = 30.8 m, as shown in Figure 5b. The associated velocity values for these two interfaces are 1500 m s^{-1} and 3600 m s^{-1}. We then draw two contour lines with velocity V = 1500 m s^{-1} and 3600 m s^{-1} in Figure 5a to represent the CZ structural boundaries for the synthetic model.

3.3. Resistivity Inversion Results

The obtained structural information is then incorporated into the regularization term (Equation 6) to improve the resistivity inversion. In the inversion, the subsurface was discretized into 3200 cells and their resistivity values were optimized using the Gauss-Newtown method. The regularization parameter λ was chosen as 50 and 1% of the logarithms of the apparent resistivity values are used as the diagonal elements in the matrix $\mathbf{W}_d$ (Günther, 2006). The optimization process was stopped after 7 iterations. The relative misfit between the observed and simulated apparent resistivity is ~0.8%. The reconstructed resistivity distribution is shown in Figure 6a. For comparison, we also conducted a traditional resistivity inversion with smoothness-based regularization, and the regularization term $\mathbf{W}_m^s$ was chosen as the second-order gradient matrix. The results of the traditional inversion are shown in Figure 6b. Note that there are some other inversion methods that can also consider subsurface structural information in the resistivity inversion, such as the image-guided inversion (Zhou et al., 2014) and the structure-based priors introduced by de Pasquale et al. (2017).

In Figures 6a and 6b, the true structural boundaries are indicated as solid lines to facilitate discussion. In general, both resistivity images show a similar pattern consistent with the true resistivity model (Figure 4c). That is, the resistivity near the ground surface is much lower than that in the deep regions (Figure 6). It is also found that the resistivity in the fractured bedrock was well reconstructed in Figure 6a using our new method. In contrast, the traditional inversion gives a very heterogeneous resistivity distribution in each CZ layer (Figure 6b). For quantitative analysis, we plot the resistivity-elevation profiles at a distance x = 65 m for both traditional and structural-constraint inversions (Figures 6a and 6b). It is clear that the resistivity curve from the new method (Figure 6a) agrees better with the true resistivity curve than the traditional method. In particular, the sharp resistivity contrast at structural boundaries (e.g., at z = 36 m and 31 m) are well reproduced in Figure 6a. We use the coefficient of determination R2 value and Lin's concordance correlation coefficient (e.g., Liao, 2003) to quantify how well the reconstructed resistivity curve agrees with the true resistivity curve. For Figures 6a and 6b (right panels), the associated R2 values are 0.990 and 0.864, and Lin's concordance correlation coefficients are 0.995 and 0.934, respectively. This confirms that the structural-constraint resistivity inversion improves the resistivity reconstruction.

3.4. Moisture Estimation Results

We apply the WS model (Equation 8) to estimate the moisture content based on the reconstructed resistivity image in Figure 6a. As discussed in section 2.4, our interpretation is different from the traditional method in two aspects. First, we use different model parameters for different structural units. Second, we do not treat each model parameter as a constant value; instead, an appropriate variation range is used. The MC simulations are conducted to calculate the mean and standard deviation of the moisture content from the resistivity image with the WS model. We treat n, ρ_{sat}, $\rho_{\mathrm{sat}}^{\mathrm{s}}$ and ϕ as random variables linearly distributed in a given range (see Table 1); that means the MC method here is based on a multivariate uniform distribution. In each MC run, these model parameters are randomly drawn from their given ranges and are then input into the WS model to convert the resistivity image into the moisture content image. In total, we conducted 10000 MC runs, and all the realizations are combined to produce the mean moisture content image (left panel of Figure 7a) and the standard deviation image (left panel of Figure 7b). The standard deviation distribution quantifies the uncertainty of estimated moisture content associated to our incomplete knowledge of the petrophysical properties of geological materials.

The mean moisture content estimated using the new method (left panel of Figure 7a) shows a similar pattern to the true moisture content distribution (Figure 4a). That is, the moisture content is relatively high in regolith and decreases to very low values in deep regions (fractured and fresh bedrocks). In addition, the estimated moisture content is also very close to the true values. For instance, the average value of the mean moisture content of the entire regolith is ~22.5%, slightly higher than the true value of 19.5%. The overall petrophysical uncertainty of the estimated moisture content is relatively small (left panel of Figure 7b). For instance, the variation range of the standard deviation in regolith is [0.02, 0.08], and it decreases to [0, 0.03] in the fresh bedrock layer. The petrophysical uncertainty shown in Figure 7a (left panel) is comparable to other borehole-based moisture content measurements such as neutron probe and nuclear magnetic resonance (e.g., Schmidt and Rempe, 2020). This implies that the moisture content could be fairly estimated from resistivity measurements if the resistivity image is reliably reconstructed and structural unit-specific petrophysical models are applied in the interpretation. In addition, we also plot the moisture content-elevation profile for the vertical transect at x = 65 m (left panel of Figure 7c). The sharp moisture content variations at the structural interfaces are clearly captured, and the estimated and true moisture content curves are in good agreement with an R2 value of 0.945 and a Lin's concordance coefficient of 0.977.

For comparison, we also estimate the moisture content based on the resistivity image in Figure 6b using the traditional method, which applies a single petrophysical model to the entire subsurface. Here we use the regolith's moisture content-resistivity relationship to interpret the entire resistivity image. Similarly, the model parameters are considered as random variables linearly distributed in a range. The calculated mean and standard deviation of the moisture content is shown in the right panel of Figure 7. It appears the traditional method still gives a similar moisture distribution pattern. However, the absolute values of the estimated moisture content deviate from the true values and have large uncertainty in the deep depth. This discrepancy can be clearly seen in the moisture content-elevation profile shown in Figure 7b (right panel), and the related R2 value is only 0.804 (Lin's concordance coefficient is 0.890).In summary, the results of the synthetic model show that the uncertainty of moisture content estimation can be significantly reduced if the structural information is incorporated in the resistivity inversion and structural unit-specific petrophysical models are used in the resistivity interpretation.

We conducted a sensitivity analysis using the Morris (1991) method, which has been successfully applied in other geoelectrical studies (e.g., Tso et al., 2020). In the analysis, the root-mean-square-error between true and estimated moisture content is used as the objective function. Based on the analysis, it is found that porosity ϕ has the largest influence on the moisture content estimation. Other parameters (such as ρ_{sat}, n, and $\rho_{\mathrm{sat}}^{\mathrm{s}}$) have the same level of influence on the moisture content estimation but are less significant than the porosity.

4. Field Example

In this section, we apply the proposed method to resistivity measurements collected near the ridge of a small catchment in the Dry Creek Experimental Watershed, Idaho, US to estimate the moisture content distribution. The details of the site condition and geophysical tests are presented. We also explain how the structural unit-specific petrophysical properties are determined. The estimated moisture content is presented and discussed to evaluate the performance of the proposed new method.

4.1. Site Condition and Geophysical Tests

The field site is within a small catchment (Figure 8) of the Dry Creek Experimental Watershed (McNamara et al., 2005) located within the Boise Front Range in semiarid southwestern Idaho, US. The bedrock of the watershed is granodiorite of Cretaceous-Paleogene age. This region was not glaciated during the Pleistocene, and soils in the region are mainly formed by in situ weathering of the underlying granite. Previous studies show that the regolith/soil layer is thin, ranging from ~10s cm to ~2 m (Poulos, 2016). The erosion rate in Idaho batholith is about 0.005 mm per year over a 10-year time scale (Kirchner et al., 2001). This indicates the residence time in the weathered profile is at the range of 200 ka, allowing regolith to have long-term exposure to weathering before being eroded.

Both electrical resistivity and seismic refraction tests have been carried out along and across a ridge of the catchment in June 2020 (Figure 8). During this time of the year, the soil/regolith layer is relatively dry, with an average volumetric moisture content of ~10% (McNamara et al., 2005). In geophysical tests, we used 72 electrodes and geophones collocated on the ground surface with a spacing of 1 m. The Syscal Pro 72 system (IRIS Instruments, Orléans, France) with the Wenner array was used to collect resistivity data, and the total number of apparent resistivity measurements are 936. We chose the Wenner array for two reasons: (1) compared to the dipole-dipole array, Wenner array has a better resolution in identifying the vertical resistivity variations (e.g., Neyamadpour et al., 2010); and (2) trial tests at this site show that the Wenner array has a higher signal-to-noise ratio than the dipole-dipole array. In the seismic tests, a sledgehammer was used to generate seismic waves at five locations along each survey line, and the Geode system (Geometrics Inc., CA, USA) was used to record the seismic responses. The shot spacing ranges between ~12 m and ~30 m and is comparable to those used in near-surface seismic refraction tests (e.g., Gallardo and Meju, 2004; Flinchum et al., 2018a). We repeated the shot 10 times at each source location to enhance the signal-to-noise ratio. The measured seismic signal of each geophone was then stacked to form a single trace, and the first arrival time was then determined. The total number of travel times is 357.

4.2. Structure Identification and Resistivity Inversion

The first arrival time data are inverted to reconstruct the velocity model for the two survey lines. In the inversion, the regularization parameter λ is chosen as 50 for the horizontal direction and 10 for the vertical direction. The data weighting matrix $\mathbf{W}_d$ is assumed as a diagonal matrix, and its elements are the inverse of 3% of the measured travel time. The inversion was stopped after 8 and 4 iterations, respectively for the profiles across and along the ridge, and the relative mean data misfits are ~4% and ~3%. The reconstructed velocity images are shown in Figures 9a and 9b. We then use the method proposed in section 2.2 to identify the boundaries of different CZ layers (Figure 9c). The regolith-fractured bedrock interface is determined as the contour line with $V = 1000$ m s^{-1}, the fractured-fresh bedrock interface as the contour line with $V = 1950$ m s^{-1}. Note that the selection of these contour values may be subjective, but a slight difference does not have a significant effect on the extracted subsurface structural interfaces. For instance, we compared contour lines with $V = 900$, 1000, and 1100 m s^{-1} for the regolith-fractured bedrock and $V = 1750$, 1950, and 2150 m s^{-1} for the fractured-fresh bedrock. The induced variation in the vertical positions (mean value) of the regolith-fractured bedrock and fractured-fresh bedrock is only ~0.6 and ~1.0 m, respectively. The fractured bedrock layer shows a clear aspect influence for the survey line across the ridge (Figure 9a). For the southeast-facing slope (left in the figure), the total thickness of regolith and fractured bedrock layers is ~15 m; in contrast, the thickness is only ~10 m for the northwest-facing slope (right in the figure). For the survey line along the ridge, the total thickness of regolith and fractured bedrock varies along the ridge from ~10 m on the right to ~20 m on the left, as shown in Figure 9b. The thickness of the regolith layer for both survey lines is between ~2 m and ~5 m, slightly higher than the augur survey results in nearby hillslopes (Poulos, 2016).

The structural information is used in the resistivity inversion to relax the smoothness constraint at the boundaries of different CZ layers. In the inversion, the smooth regularization parameter λ is 5; the data weighting matrix is assumed as diagonal, and the element is the inverse of 4% (6%) of the measured apparent resistivity along (across) the ridge. Both inversions were stopped after 4 iterations, and the related relative data misfits are respectively ~10% and ~3% for the survey lines across and along the ridge. The resistivity inversion results are shown in Figure 10.

4.3. Moisture Content Results and Discussion

To interpret the resistivity distribution, we need to determine the variation ranges of the model parameters in Equation 8 for the site. In this study, we use existing experimental data of samples collected at the site and published data of other similar materials to constrain these model parameters. For porosity ϕ, the material near the ground surface has

been measured, ranging between ~30% and ~50% (Geroy et al., 2011). Considering the decreasing trend of ϕ with depth in the regolith (Hayes et al., 2019), we therefore assume the variation range is from 25% to 50% (see Table 2). The stream water conductivity σ_w at the site is monitored year-round, and it generally varies between 0.01 and 0.025 S m^{-1}. Regolith samples were collected from a soil pit along the ridge at x = 14 m, and their apparent formation factor F_a (ratio of saturated resistivity over pore water resistivity) was found to vary between 1.3 and 2.8 (Bienvenue, 2021). Note that the low F_a values are due to the presence of clay minerals (up to ~40% by weight; Bienvenue, 2021). Using σ_w = 0.02 S m^{-1}, ϕ in the range of [25%, 50%], and measured F_a values, we can determine that the range of the saturated resistivity ρ_{sat} of the regolith varies between 50 and 250 Ω m. The saturated resistivity of the regolith related to surface conduction ρ_{sat}^{s} was estimated from lab experimental data, and it was in the range between 400 and 3200 Ω m. The saturation exponent n of regolith samples is assumed to vary between 1.3 and 2.2, a typical range for relatively coarse granular materials (e.g., Doussan and Ruy, 2009).

For the porosity of fractured bedrock, direct field measurement data are not available. Results from a site with similar geology (Rempe and Dietrich, 2018) indicate that although the pore volume in fractured granite is lower than the regolith developed on bedrock, the porosity is still substantial, averaging ~25%. Thus, we assume the porosity of the fractured bedrock in our site ranges between 15% and 30%. Assuming the cementation factor m ranges between 1 and 1.2, a typical value for fractured materials (e.g., Yue, 2019), we estimate ρ_{sat} of the fractured bedrock at our site is between 165 and 350 Ωm (Table 2). Surface conduction is not considered for both the fractured and fresh bedrock. The porosity of intact granite is ~1% (e.g., Llera et al., 1990). Considering the presence of microfractures, we assume the porosity of the fresh bedrock at our site ranges between 5% and 15%, similar to the observations of a granitic gneiss site in Holbrook et al. (2019). We estimate the cementation exponent m of the fresh bedrock using the experimental data in Llera et al. (1990), and it gives a value close to 1. Based on m and ϕ, we can estimate that the range of ρ_{sat} for the fresh bedrock is between 325 to 1000 Ω m (Table 2). For the saturation exponent n, we simply assume $n = m + 1$ (Mualem and Friedman, 1991). All the parameters are summarized in Table 2.

Using Archie's law and the model parameters in Table 2, we estimate the mean and standard deviation of the moisture content for the field site based on the resistivity image in Figure 10 using the MC simulation. The results are shown in Figures 11a and 11b, respectively, for survey lines across and along the ridge. The two moisture content images in Figure 11 show similar patterns. First, shallow regolith (<1 m) has a relatively low moisture content, ~16%. This dry layer is the result of a combined effect of the high evaporation/evapotranspiration rate and low precipitation at the site in the summer (McNamara et al., 2018). Second, the perched water, an important subsurface water component in runoff generation (e.g., Guo et al., 2019; McDonnell et al., 2021), is clearly seen at the regolith-fractured bedrock interfaces. For instance, the moisture content at the regolith-fractured bedrock interface is considerably high in the right panel of Figure 11a at x = 17 m, exceeding ~40%. This perched water also coincides with the location of a conifer tree (at x = 18) on the ridge. In the fractured bedrock, the moisture content is relatively high, ranging between ~15% and ~30%. This component of groundwater (i.e., rock moisture) was historically overlooked in hydrologic studies, but recent studies have highlighted its importance in supporting vegetation evapotranspiration during dry seasons (Rempe and Dietrich, 2018). Within the fractured bedrock, small patches with relatively high moisture content can also be found, for example, at x = 45 in the left panel of Figure 11a and x = 38 m and 55 m in the right panel of Figure 11a. These relatively wet regions connect the regolith (soil) water to fresh bedrock and thus may be the preferential flow path that facilitates the bedrock infiltration (Kormos et al., 2015). The petrophysical uncertainties related to the moisture content estimation are shown in Figure 11b. In general, the uncertainty varies within different CZ layers, decreasing from ~10% in regolith to ~ 2% in the bedrock. This decreased uncertainty in deep depth is associated with the smaller variability of resistivity model parameters in bedrocks. This result implies that if the petrophysical properties of a structural unit can be better understood, the uncertainty related to resistivity-estimated moisture content could be reduced.

4.4. Comparison with the Traditional Method

We also estimate the moisture content of the field site from resistivity measurements using the traditional methods. It is noted that, in the traditional method, no structural information was used to constrain the resistivity inversion, and the petrophysical relationship of the regolith is used for the moisture interpretation of the entire subsurface. We selected the moisture content-elevation profiles of two representative transects (x = 45 m across the ridge and x = 17 along the ridge) for a direct comparison of the traditional and new methods. As shown in Figure 12, the new method clearly reveals the sharp moisture contrasts at CZ boundaries, which have been observed in other granitic CZs (e.g.,

Flinchum et al., 2019). For example, the sudden decrease in moisture content at z = 1633 in Figure 12 b was not captured with the traditional method. Thus, the traditional method may not identify the perched water at the regolith-fractured bedrock interface.

Moreover, using a single petrophysical relationship for all the three CZ layers significantly overestimates the moisture content in fractured and fresh bedrocks. For instance, the traditional method gives a moisture content of ~20% for rocks ~20 m below the ridge in Figure 12a. In this deep depth, the microfractures in the bedrock are less likely to open due to the high confining pressure (supported by the large velocity value, exceeding ~3000 m s^{-1}). Thus, the moisture stored in deep bedrocks should be limited, consistent with the results of the new method. Direct rock moisture measurements at the site would help validate our interpretation. Unfortunately, no boreholes are installed at the site. Further studies are recommended to drill boreholes and conduct borehole geophysical logging (e.g., neutron probe or nuclear magnetic resonance) such that direct observations of rock moisture can be realized.

Lastly, we comment on the field conditions where the proposed method should be used. If the subsurface structure is known to be strongly heterogeneous such as at mountainous CZ sites, it is always preferred to use structural information to constrain the moisture content estimation. However, if the sites are only slightly heterogeneous such as at unconsolidated aquifers or agricultural fields, it is expected that the structural boundaries are not clearly defined and may not be identified with seismic refraction tomography. Under these conditions, using structural information may not improve the moisture content estimation. Of course, the cost is also a concern because both seismic refraction tests in the field and structural-based resistivity inversion are more costly than the traditional methods.

5. Conclusions

In this study, we proposed to use the subsurface structural information to reduce the uncertainty of moisture content estimation with field resistivity measurements. The results of the synthetic subsurface example show that seismic refraction tomography contains enough structural information, which can be extracted with the velocity gradient-based method from the reconstructed velocity images. Incorporating the structural information into resistivity inversions can relax the regularization-forced smoothing at structural boundaries, thus improving the reconstruction of resistivity images. In particular, the sharp resistivity contrast near structural boundaries is better captured if compared to traditional inversion. The synthetic example also shows that the moisture content estimated using structural unit-specific petrophysical models gives a similar spatial pattern as the true model. In addition to spatial patterns, the estimated moisture content values with the new method agree very well with the true moisture content. Compared to the traditional method that applies a single petrophysical relationship to the entire subsurface, the new method shows a better performance.

The new method has been applied to a granitic hillslope to estimate the moisture content distribution from field resistivity measurements. The resistivity-estimated moisture content distributions exhibit typical features commonly found in hillslopes, such as perched water at the soil/rock interface and preferential flow path contributing to groundwater recharge. Although no ground truth is available for validating the estimated moisture content, a comparison with the traditional method results confirms our proposed methods' superior performance. Therefore, we conclude that incorporating structural information in resistivity inversion and using structural unit-specific petrophysical models can improve the estimation of subsurface moisture content from field resistivity measurements. Therefore, if the subsurface is strongly heterogeneous in structure, for example, at mountainous CZ sites, it is preferred to adopt this new method. However, if the sites are only slightly heterogeneous, this new method may not be able to improve the moisture content estimation from resistivity tomography.

Reference

Ackerer, J., Ranchoux, C., Lucas, Y., Viville, D., Clément, A., Fritz, B., Lerouge, C., Schäfer, G. and Chabaux, F., 2021. Investigating the role of deep weathering in critical zone evolution by reactive transport modeling of the geochemical composition of deep fracture water. *Geochimica et Cosmochimica Acta*, 312, pp.257-278.

Aster, R., Borchers, B., and Thurber, C. H., 2005. Parameter estimation and inverse problems. Burlington, Massachusetts, USA: Elsevier.

Befus, K.M., Sheehan, A.F., Leopold, M., Anderson, S.P. and Anderson, R.S., 2011. Seismic constraints on critical zone architecture, Boulder Creek watershed, Front Range, Colorado. *Vadose Zone Journal*, *10*(3), pp.915-927.

Benninga, H.J.F., Carranza, C.D., Pezij, M., van Santen, P., van der Ploeg, M.J., Augustijn, D. and van der Velde, R., 2018. The Raam regional soil moisture monitoring network in the Netherlands. *Earth system science data*, 10(1), pp.61-79.

Berre, I., Doster, F. and Keilegavlen, E., 2019. Flow in fractured porous media: A review of conceptual models and discretization approaches. *Transport in Porous Media*, 130(1), pp.215-236.

Berryman, J.G., 1992. Single-scattering approximations for coefficients in Biot's equations of poroelasticity. *The Journal of the Acoustical Society of America*, 91(2), pp.551-571.

Bienvenue, T.J., 2021. *Laboratory Measurement of Electrical and Hydraulic Properties of Regolith over Granitic Bedrock* (Master Thesis, Boise State University).

Binley, A., Hubbard, S.S., Huisman, J.A., Revil, A., Robinson, D.A., Singha, K. and Slater, L.D., 2015. The emergence of hydrogeophysics for improved understanding of subsurface processes over multiple scales. *Water resources research*, *51*(6), pp.3837-3866.

Boadu, F.K. and Long, L.T., 1996. Effects of fractures on seismic-wave velocity and attenuation. *Geophysical Journal International*, 127(1), pp.86-110.

Boadu, F.K., 1998. Inversion of fracture density from field seismic velocities using artificial neural networks. *Geophysics*, 63(2), pp.534-545.

Brooks, E.S., Saia, S.M., Boll, J., Wetzel, L., Easton, Z.M. and Steenhuis, T.S., 2015. Assessing BMP Effectiveness and Guiding BMP Planning Using Process-Based Modeling. *JAWRA Journal of the American Water Resources Association*, *51*(2), pp.343-358.

Brunetti, C., Linde, N. and Vrugt, J.A., 2017. Bayesian model selection in hydrogeophysics: Application to conceptual subsurface models of the South Oyster Bacterial Transport Site, Virginia, USA. *Advances in Water Resources*, 102, pp.127-141.

Brunetti, C. and Linde, N., 2018. Impact of petrophysical uncertainty on Bayesian hydrogeophysical inversion and model selection. *Advances in Water Resources*, 111, pp.346-359.

Chen, H. and Niu, Q., 2021, December. Influence of subsurface heterogeneity on critical zone characterizations with electrical resistivity and seismic refraction tomography. In *Sixth International Conference on Engineering Geophysics, Virtual, 25–28 October 2021* (pp. 213-216). Society of Exploration Geophysicists.

Constable, S., 2010. Ten years of marine CSEM for hydrocarbon exploration. *Geophysics*, 75(5), pp.75A67-75A81.

Constable, S.C., Parker, R.L. and Constable, C.G., 1987. Occam's inversion: A practical algorithm for generating smooth models from electromagnetic sounding data. *Geophysics*, 52(3), pp.289-300.

Coscia, I., Greenhalgh, S.A., Linde, N., Doetsch, J., Marescot, L., Günther, T., Vogt, T. and Green, A.G., 2011. 3D crosshole ERT for aquifer characterization and monitoring of infiltrating river water. *Geophysics*, 76(2), pp.G49-G59.

Day-Lewis, F.D., Linde, N., Haggerty, R., Singha, K. and Briggs, M.A., 2017. Pore network modeling of the electrical signature of solute transport in dual-domain media. *Geophysical Research Letters*, *44*(10), pp.4908-4916.

de Pasquale, G. and Linde, N., 2017. On structure-based priors in Bayesian geophysical inversion. *Geophysical Journal International*, 208(3), pp.1342-1358.

de Pasquale, G., Linde, N., Doetsch, J. and Holbrook, W.S., 2019. Probabilistic inference of subsurface heterogeneity and interface geometry using geophysical data. *Geophysical Journal International*, 217(2), pp.816-831.

Dobriyal, P., Qureshi, A., Badola, R. and Hussain, S.A., 2012. A review of the methods available for estimating soil moisture and its implications for water resource management. *Journal of Hydrology*, 458, pp.110-117.

Doetsch, J., Linde, N., Pessognelli, M., Green, A.G. and Günther, T., 2012. Constraining 3-D electrical resistance tomography with GPR reflection data for improved aquifer characterization. *Journal of Applied Geophysics*, *78*, pp.68-76.

Doetsch, J., Linde, N. and Binley, A., 2010. Structural joint inversion of time-lapse crosshole ERT and GPR traveltime data. *Geophysical research letters*, 37(24).

Dorigo, W., Van Oevelen, P., Wagner, W., Drusch, M., Mecklenburg, S., Robock, A. and Jackson, T., 2011. A new international network for in situ soil moisture data. Eos, *Transactions American Geophysical Union*, 92(17), pp.141-142.

Doussan, C. and Ruy, S., 2009. Prediction of unsaturated soil hydraulic conductivity with electrical conductivity. *Water Resources Research*, *45*(10).

Falcon-Suarez, I.H., North, L., Callow, B., Bayrakci, G., Bull, J. and Best, A., 2020. Experimental assessment of the stress-sensitivity of combined elastic and electrical anisotropy in shallow reservoir sandstones. *Geophysics*, 85(5), pp.MR271-MR283.

Flinchum, B.A., Holbrook, W., Rempe, D., Moon, S., Riebe, C.S., Carr, B.J., Hayes, J.L., St. Clair, J. and Peters, M.P., 2018a. Critical zone structure under a granite ridge inferred from drilling and three-dimensional seismic refraction data. *Journal of Geophysical Research: Earth Surface*, 123(6), pp.1317-1343.

Flinchum, B.A., Holbrook, W.S., Grana, D., Parsekian, A.D., Carr, B.J., Hayes, J.L. and Jiao, J., 2018b. Estimating the water holding capacity of the critical zone using near-surface geophysics. *Hydrological Processes*, *32*(22), pp.3308-3326.

Flinchum, B.A., Holbrook, W.S., Parsekian, A.D. and Carr, B.J., 2019. Characterizing the critical zone using borehole and surface nuclear magnetic resonance. *Vadose Zone Journal*, *18*(1), pp.1-18.

Friedman, S.P., 2005. Soil properties influencing apparent electrical conductivity: a review. *Computers and electronics in agriculture*, 46(1-3), pp.45-70.

Gallardo, L.A. and Meju, M.A., 2004. Joint two-dimensional DC resistivity and seismic travel time inversion with cross-gradients constraints. *Journal of Geophysical Research: Solid Earth*, *109*(B3).

Garré, S., Javaux, M., Vanderborght, J., Pagès, L. and Vereecken, H., 2011. Three-dimensional electrical resistivity tomography to monitor root zone water dynamics. *Vadose Zone Journal*, 10(1), pp.412-424.

Geroy, I.J., Gribb, M.M., Marshall, H.P., Chandler, D.G., Benner, S.G. and McNamara, J.P., 2011. Aspect influences on soil water retention and storage. *Hydrological Processes*, *25*(25), pp.3836-3842.

Ghanbarian, B., Hunt, A.G., Ewing, R.P. and Skinner, T.E., 2014. Universal scaling of the formation factor in porous media derived by combining percolation and effective medium theories. *Geophysical Research Letters*, 41(11), pp.3884-3890.

Glover, P.W., 2017. A new theoretical interpretation of Archie's saturation exponent. *Solid Earth*, *8*(4), pp.805-816.

González, J.A.M., Comte, J.C., Legchenko, A., Ofterdinger, U. and Healy, D., 2021. Quantification of groundwater storage heterogeneity in weathered/fractured basement rock aquifers using electrical resistivity tomography: Sensitivity and uncertainty associated with petrophysical modelling. Journal of Hydrology, 593, p.125637.

Günther, T., Rücker, C. and Spitzer, K., 2006. Three-dimensional modelling and inversion of DC resistivity data incorporating topography—II. Inversion. *Geophysical Journal International*, *166*(2), pp.506-517.

Guo, L., Lin, H., Fan, B., Nyquist, J., Toran, L. and Mount, G.J., 2019. Preferential flow through shallow fractured bedrock and a 3D fill-and-spill model of hillslope subsurface hydrology. *Journal of Hydrology*, *576*, pp.430-442.

Hahm, W.J., Rempe, D.M., Dralle, D.N., Dawson, T.E. and Dietrich, W.E., 2020. Oak transpiration drawn from the weathered bedrock vadose zone in the summer dry season. *Water Resources Research*, 56(11), p.e2020WR027419.

Han, L. and Showman, A.P., 2008. Implications of shear heating and fracture zones for ridge formation on Europa. *Geophysical Research Letters*, *35*(3).

Hayes, J.L., Riebe, C.S., Holbrook, W.S., Flinchum, B.A. and Hartsough, P.C., 2019. Porosity production in weathered rock: Where volumetric strain dominates over chemical mass loss. *Science advances*, *5*(9), p.eaao0834.

Heimovaara, T.J. and Bouten, W., 1990. A computer-controlled 36-channel time domain reflectometry system for monitoring soil water contents. *Water Resources Research*, 26(10), pp.2311-2316.

Holbrook, W.S., Marcon, V., Bacon, A.R., Brantley, S.L., Carr, B.J., Flinchum, B.A., Richter, D.D. and Riebe, C.S., 2019. Links between physical and chemical weathering inferred from a 65-m-deep borehole through Earth's critical zone. *Scientific reports*, 9(1), pp.1-11.

Jiang, C., Igel, J., Dlugosch, R., Müller-Petke, M., Günther, T., Helms, J., Lang, J. and Winsemann, J., 2020. Magnetic resonance tomography constrained by ground-penetrating radar for improved hydrogeophysical characterization. *Geophysics*, 85(6), pp.JM13-JM26.

Jiang, W. and Zhang, J., 2017. First-arrival traveltime tomography with modified total-variation regularization. *Geophysical Prospecting*, 65(5), pp.1138-1154.

Johnson, T.C., Slater, L.D., Ntarlagiannis, D., Day-Lewis, F.D. and Elwaseif, M., 2012. Monitoring groundwater-surface water interaction using time-series and time-frequency analysis of transient three-dimensional electrical resistivity changes. *Water Resources Research*, 48(7).

Jordi, C., Doetsch, J., Günther, T., Schmelzbach, C. and Robertsson, J.O., 2018. Geostatistical regularization operators for geophysical inverse problems on irregular meshes. *Geophysical Journal International*, *213*(2), pp.1374-1386.

Kirchner, J.W., Finkel, R.C., Riebe, C.S., Granger, D.E., Clayton, J.L., King, J.G. and Megahan, W.F., 2001. Mountain erosion over 10 yr, 10 ky, and 10 my time scales. *Geology*, *29*(7), pp.591-594.

Kormos, P.R., McNamara, J.P., Seyfried, M.S., Marshall, H.P., Marks, D. and Flores, A.N., 2015. Bedrock infiltration estimates from a catchment water storage-based modeling approach in the rain snow transition zone. *Journal of Hydrology*, *525*, pp.231-248.

Laloy, E., Javaux, M., Vanclooster, M., Roisin, C. and Bielders, C.L., 2011. Electrical resistivity in a loamy soil: Identification of the appropriate pedo-electrical model. *Vadose Zone Journal*, 10(3), pp.1023-1033.

Leopold, M., Gupanis-Broadway, C., Baker, A., Hankin, S. and Treble, P., 2021. Time lapse electric resistivity tomography to portray infiltration and hydrologic flow paths from surface to cave. *Journal of Hydrology*, 593, p.125810.

Lesmes, D.P. and Friedman, S.P., 2005. Relationships between the electrical and hydrogeological properties of rocks and soils. In *Hydrogeophysics* (pp. 87-128). Springer, Dordrecht.

Liao, J.J., 2003. An improved concordance correlation coefficient. *Pharmaceutical Statistics: The Journal of Applied Statistics in the Pharmaceutical Industry*, 2(4), pp.253-261.

Linde, N. and Doetsch, J., 2016. Joint inversion in hydrogeophysics and near-surface geophysics. *Integrated imaging of the Earth: Theory and applications*, *218*, pp.119-135.

Linde, N., Ginsbourger, D., Irving, J., Nobile, F. and Doucet, A., 2017. On uncertainty quantification in hydrogeology and hydrogeophysics. *Advances in Water Resources*, 110, pp.166-181.

Llera, F.J., Sato, M., Nakatsuka, K. and Yokoyama, H., 1990. Temperature dependence of the electrical resistivity of water-saturated rocks. *Geophysics*, *55*(5), pp.576-585.

Mavko, G., Mukerji, T. and Dvorkin, J., 2020. *The rock physics handbook*. Cambridge university press.

McDonnell, J.J., Spence, C., Karran, D.J., Van Meerveld, H.J. and Harman, C.J., 2021. Fill-and-spill: A process description of runoff generation at the scale of the beholder. *Water Resources Research*, *57*(5), p.e2020WR027514.

McNamara, J.P., Benner, S.G., Poulos, M.J., Pierce, J.L., Chandler, D.G., Kormos, P.R., Marshall, H.P., Flores, A.N., Seyfried, M., Glenn, N.F. and Aishlin, P., 2018. Form and function relationships revealed by long-term research in a semiarid mountain catchment. *Wiley Interdisciplinary Reviews: Water*, *5*(2), p.e1267.

McNamara, J.P., Chandler, D., Seyfried, M. and Achet, S., 2005. Soil moisture states, lateral flow, and streamflow generation in a semi-arid, snowmelt-driven catchment. *Hydrological Processes: An International Journal*, *19*(20), pp.4023-4038.

Mohanty, B.P., Cosh, M.H., Lakshmi, V. and Montzka, C., 2017. Soil moisture remote sensing: State-of-the-science. *Vadose Zone Journal*, 16(1), pp.1-9.

Morris, M.D., 1991. Factorial sampling plans for preliminary computational experiments. *Technometrics*, 33(2), pp.161-174.

Mualem, Y. and Friedman, S.P., 1991. Theoretical prediction of electrical conductivity in saturated and unsaturated soil. *Water Resources Research*, *27*(10), pp.2771-2777.

Neyamadpour, A., Wan Abdullah, W.A.T., Taib, S. and Neyamadpour, B., 2010. Comparison of Wenner and dipole–dipole arrays in the study of an underground three-dimensional cavity. *Journal of Geophysics and Engineering*, *7*(1), pp.30-40.

Niu, Q., Fratta, D. and Wang, Y.H., 2015. The use of electrical conductivity measurements in the prediction of hydraulic conductivity of unsaturated soils. *Journal of Hydrology*, 522, pp.475-487.

Olona, J., Pulgar, J.A., Fernández-Viejo, G., López-Fernández, C. and González-Cortina, J.M., 2010. Weathering variations in a granitic massif and related geotechnical properties through seismic and electrical resistivity methods. *Near Surface Geophysics*, *8*(6), pp.585-599.

Parsekian, A.D., Singha, K., Minsley, B.J., Holbrook, W.S. and Slater, L., 2015. Multiscale geophysical imaging of the critical zone. *Reviews of Geophysics*, *53*(1), pp.1-26.

Pasquet, S., Holbrook, W. S., Carr, B. J., & Sims, K. W. W. (2016). Geophysical imaging of shallow degassing in a Yellowstone hydrothermal system. Geophysical Research Letters, 43(23), 12-027.

Perrone, A., Lapenna, V. and Piscitelli, S., 2014. Electrical resistivity tomography technique for landslide investigation: A review. *Earth-Science Reviews*, *135*, pp.65-82.

Pidlisecky, A. and Knight, R., 2008. FW2_5D: A MATLAB 2.5-D electrical resistivity modeling code. *Computers & Geosciences*, *34*(12), pp.1645-1654.

Pleasants, M.S., Neves, F.D.A., Parsekian, A.D., Befus, K.M. and Kelleners, T.J., 2022. Hydrogeophysical Inversion of Time-Lapse ERT Data to Determine Hillslope Subsurface Hydraulic Properties. *Water Resources Research*, 58(4), p.e2021WR031073.

Pope, G.A., 2015. Regolith and weathering (rock decay) in the critical zone. In *Developments in Earth Surface Processes* (Vol. 19, pp. 113-145). Elsevier.

Poulos, M.J., 2016. Feedbacks Among Climate, Soils, Vegetation, and Erosion Drive Valley Asymmetry Development in the Mountains of Central Idaho. (*Doctoral dissertation*, Boise State University).

Pride, S. R. (2005). Relationships between seismic and hydrological properties. In Hydrogeophysics (pp. 253-290). Springer, Dordrecht.

Romero-Ruiz, A., Linde, N., Baron, L., Breitenstein, D., Keller, T. and Or, D., 2022. Lasting effects of soil compaction on soil water regime confirmed by geoelectrical monitoring. *Water Resources Research*, 58(2), p.e2021WR030696.

Rempe, D.M. and Dietrich, W.E., 2018. Direct observations of rock moisture, a hidden component of the hydrologic cycle. *Proceedings of the National Academy of Sciences*, *115*(11), pp.2664-2669.

Revil, A. and Glover, P.W.J., 1998. Nature of surface electrical conductivity in natural sands, sandstones, and clays. *Geophysical research letters*, *25*(5), pp.691-694.

Robinson, D.A., Campbell, C.S., Hopmans, J.W., Hornbuckle, B.K., Jones, S.B., Knight, R., Ogden, F., Selker, J. and Wendroth, O., 2008. Soil moisture measurement for ecological and hydrological watershed-scale observatories: A review. *Vadose Zone Journal*, 7(1), pp.358-389.

Roy, A., 1962. Ambiguity in geophysical interpretation. *Geophysics*, *27*(1), pp.90-99.

Rücker, C., 2010. Advanced electrical resistivity modelling and inversion using unstructured discretization (*Doctoral dissertation*, Universität Leipzig).

Rücker, C., Günther, T. and Wagner, F.M., 2017. pyGIMLi: An open-source library for modelling and inversion in geophysics. *Computers & Geosciences*, *109*, pp.106-123.

Sánchez, N., Martínez-Fernández, J., Calera, A., Torres, E. and Pérez-Gutiérrez, C., 2010. Combining remote sensing and in situ soil moisture data for the application and validation of a distributed water balance model (HIDROMORE). *Agricultural Water Management*, 98(1), pp.69-78.

Schmidt, L. and Rempe, D., 2020. Quantifying dynamic water storage in unsaturated bedrock with borehole nuclear magnetic resonance. *Geophysical Research Letters*, 47(22), p.e2020GL089600.

Schön, J.H., 2015. *Physical properties of rocks: Fundamentals and principles of petrophysics*. Elsevier.

Sen, P.N., Scala, C. and Cohen, M.H., 1981. A self-similar model for sedimentary rocks with application to the dielectric constant of fused glass beads. *Geophysics*, 46(5), pp.781-795.

Skibbe, N., Günther, T. and Müller-Petke, M., 2021. Improved hydrogeophysical imaging by structural coupling of 2D magnetic resonance and electrical resistivity tomography. *Geophysics*, *86*(5), pp.WB77-WB88.

Slater, L. and Binley, A., 2021. Advancing hydrological process understanding from long-term resistivity monitoring systems. *Wiley Interdisciplinary Reviews: Water*, 8(3), p.e1513.

Slater, L. and Binley, A., 2006. Synthetic and field-based electrical imaging of a zerovalent iron barrier: Implications for monitoring long-term barrier performance. *Geophysics*, 71(5), pp.B129-B137.

St. Clair, J., Moon, S., Holbrook, W.S., Perron, J.T., Riebe, C.S., Martel, S.J., Carr, B., Harman, C., Singha, K.D. and Richter, D.D., 2015. Geophysical imaging reveals topographic stress control of bedrock weathering. *Science*, *350*(6260), pp.534-538.

Tso, C.H.M., Kuras, O. and Binley, A., 2019. On the field estimation of moisture content using electrical geophysics: The impact of petrophysical model uncertainty. *Water Resources Research*, *55*(8), pp.7196-7211.

Tso, C.H.M., Iglesias, M., Wilkinson, P., Kuras, O., Chambers, J. and Binley, A., 2021. Efficient multiscale imaging of subsurface resistivity with uncertainty quantification using ensemble Kalman inversion. *Geophysical Journal International*, 225(2), pp.887-905.

Tso, C.H.M., Johnson, T.C., Song, X., Chen, X., Kuras, O., Wilkinson, P., Uhlemann, S., Chambers, J. and Binley, A., 2020. Integrated hydrogeophysical modelling and data assimilation for geoelectrical leak detection. *Journal of Contaminant Hydrology*, 234, p.103679.

Van Avendonk, H.J., Shillington, D.J., Holbrook, W.S. and Hornbach, M.J., 2004. Inferring crustal structure in the Aleutian island arc from a sparse wide-angle seismic data set. *Geochemistry, Geophysics, Geosystems*, 5(8).

Vauhkonen, M., Vadasz, D., Karjalainen, P.A., Somersalo, E. and Kaipio, J.P., 1998. Tikhonov regularization and prior information in electrical impedance tomography. *IEEE transactions on medical imaging*, *17*(2), pp.285-293.

Vischel, T., Pegram, G.G.S., Sinclair, S., Wagner, W. and Bartsch, A., 2008. Comparison of soil moisture fields estimated by catchment modelling and remote sensing: a case study in South Africa. *Hydrology and Earth System Sciences*, 12(3), pp.751-767.

Wagner, F.M. and Uhlemann, S., 2021. An overview of multimethod imaging approaches in environmental geophysics. *Advances in Geophysics*, *62*, pp.1-72.

Wan, J., Tokunaga, T.K., Williams, K.H., Dong, W., Brown, W., Henderson, A.N., Newman, A.W. and Hubbard, S.S., 2019. Predicting sedimentary bedrock subsurface weathering fronts and weathering rates. *Scientific reports*, *9*(1), pp.1-10.

Waxman, M.H. and Smits, L.J.M., 1968. Electrical conductivities in oil-bearing shaly sands. *Society of Petroleum Engineers Journal*, 8(02), pp.107-122.

Wellmann, J.F., De La Varga, M., Murdie, R.E., Gessner, K. and Jessell, M., 2018. Uncertainty estimation for a geological model of the Sandstone greenstone belt, Western Australia–insights from integrated geological and geophysical inversion in a Bayesian inference framework. *Geological Society, London, Special Publications*, *453*(1), pp.41-56.

Wesson, R.L., 1971. Travel-time inversion for laterally inhomogeneous crustal velocity models. *Bulletin of the Seismological Society of America*, *61*(3), pp.729-746.

Western, A.W., Zhou, S.L., Grayson, R.B., McMahon, T.A., Blöschl, G. and Wilson, D.J., 2004. Spatial correlation of soil moisture in small catchments and its relationship to dominant spatial hydrological processes. *Journal of Hydrology*, 286(1-4), pp.113-134.

White, D.J., 1989. Two-dimensional seismic refraction tomography. *Geophysical Journal International*, *97*(2), pp.223-245.

Wisén, R., Auken, E. and Dahlin, T., 2005. Combination of 1D laterally constrained inversion and 2D smooth inversion of resistivity data with a priori data from boreholes. *Near Surface Geophysics*, 3(2), pp.71-79.

Yue, Z., Song, Y., Li, P., Tian, S., Ming, X. and Chen, Z., 2019. Applications of digital image correlation (DIC) and the strain gage method for measuring dynamic mode I fracture parameters of the white marble specimen. *Rock Mechanics and Rock Engineering*, *52*(11), pp.4203-4216.

Zhang, J. and Toksöz, M.N., 1998. Nonlinear refraction traveltime tomography. *Geophysics*, 63(5), pp.1726-1737.

Zhang, Z.F., Ward, A.L. and Gee, G.W., 2003. A tensorial connectivity–tortuosity concept to describe the unsaturated hydraulic properties of anisotropic soils. *Vadose Zone Journal*, *2*(3), pp.313-321.

Zhdanov, M.S., 2002. *Geophysical inverse theory and regularization problems* (Vol. 36). Elsevier.

Zhou, J., Revil, A., Karaoulis, M., Hale, D., Doetsch, J. and Cuttler, S., 2014. Image-guided inversion of electrical resistivity data. *Geophysical Journal International*, *197*(1), pp.292-309.

Zhukov, V.S. and Kuzmin, Y.O., 2020. The Influence of Fracturing of the Rocks and Model Materials on P-Wave Propagation Velocity: Experimental Studies. Izvestiya, *Physics of the Solid Earth*, 56(4), pp.470-480.

Figures

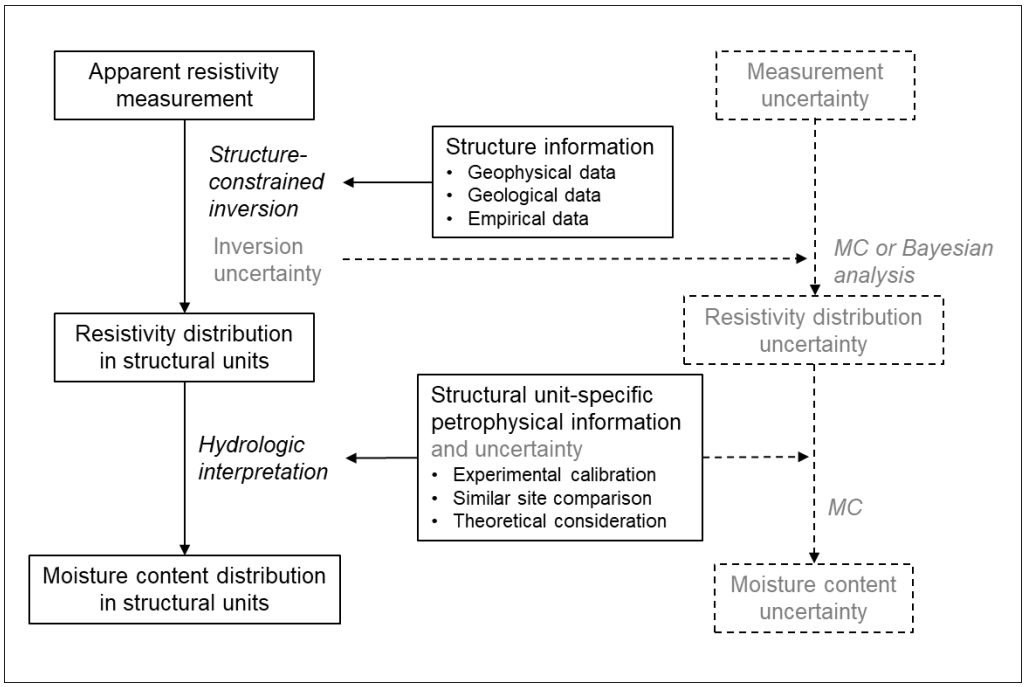

Figure 1. The proposed workflow for estimating moisture content from field resistivity measurements and evaluating relevant uncertainties. MC stands for Monte Carlo analysis.

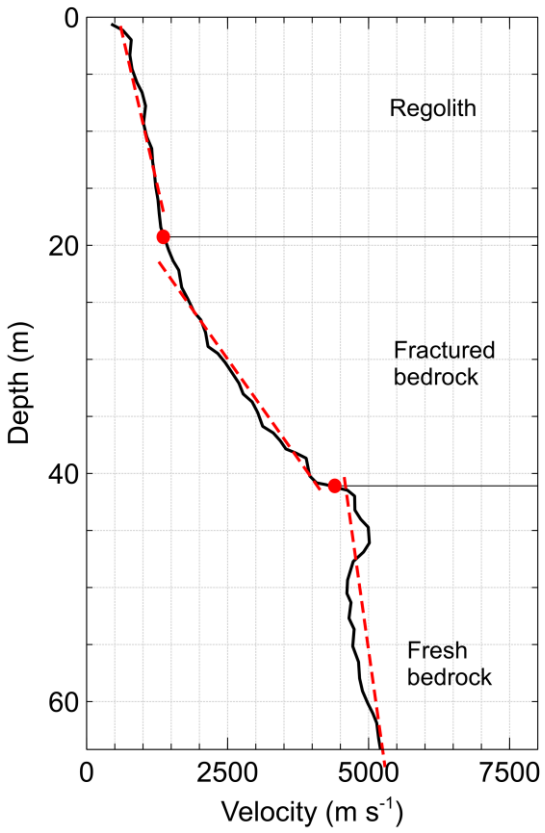

Figure 2. The proposed method for identifying the critical zone layers (regolith, fractured bedrock, and fresh bedrock) from a velocity-depth profile. Depths with distinct velocity gradients are identified as different structural units. The velocity-depth data are from Flinchum et al (2022). Red dash lines are used to represent constant velocity gradients.

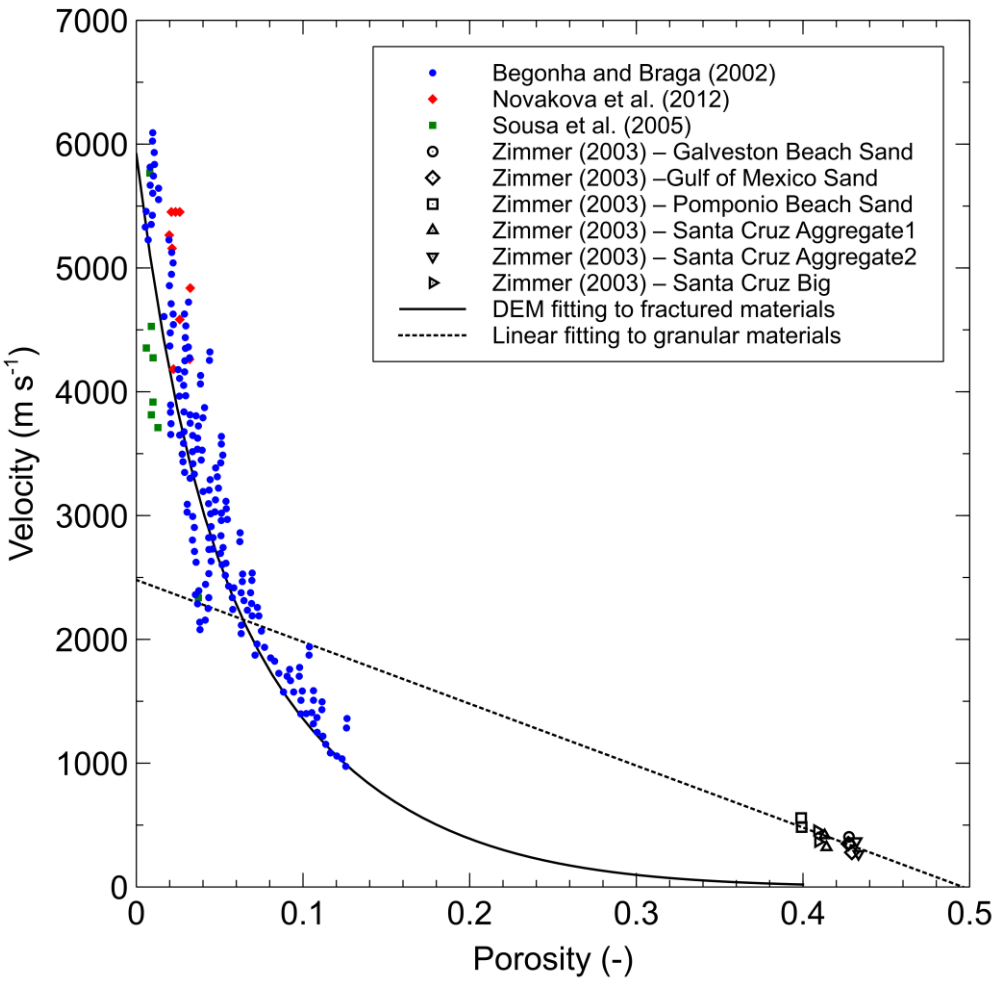

Figure 3. The p-wave velocity-porosity relationships for granular and fractured geological materials. The differential effective medium (DEM) theory (Berryman et al., 2002) is used to fit the fractured materials (solid line), and the linear empirical model (Han et al., 1986) is used to fit the granular materials (dash line). For velocity data in Zimmer (2003), only those with a low confining pressure are used in the above figure.

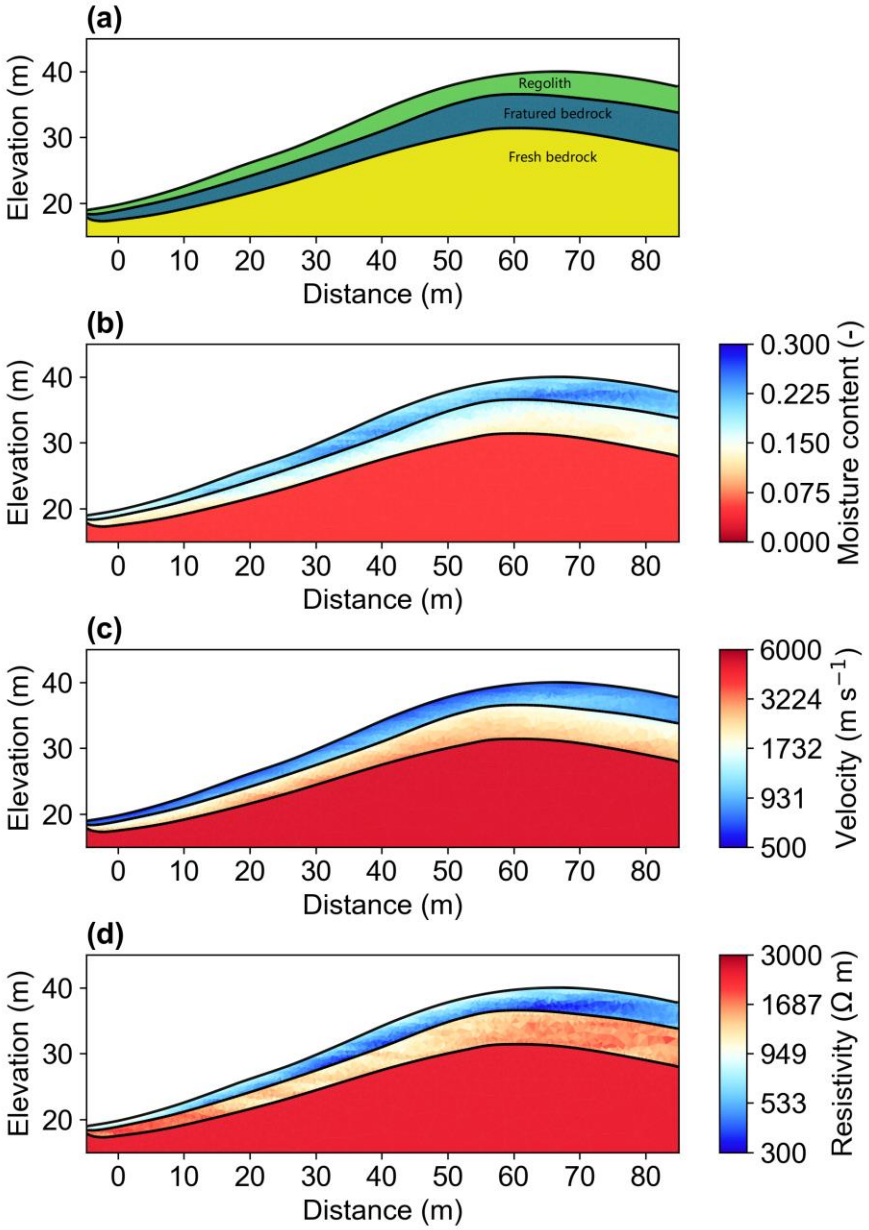

Figure 4. Synthetic subsurface model: (a) structural units, (b) moisture content distribution, (c) velocity distribution, and (d) resistivity distribution.

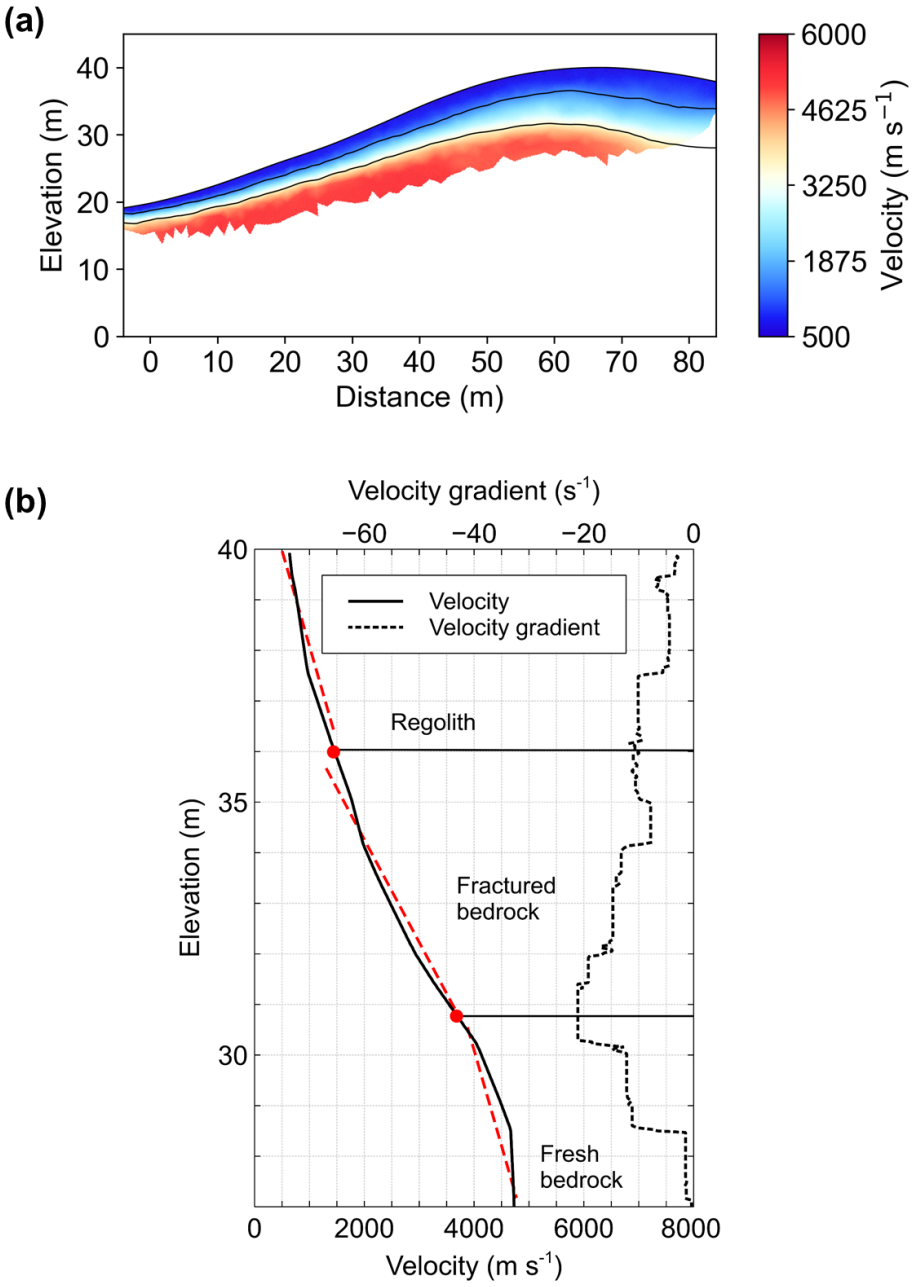

Figure 5. The reconstructed velocity distribution of the synthetic model: (a) spatial distribution and (b) velocity and velocity gradient profiles for vertical transect at distance x = 68 m. The identified CZ structural boundaries are indicated by solid lines in (a) and represented by red dots and horizontal lines in (b). The associated velocity for the regolith-fractured bedrock interface is 1500 m s^{-1} and is 3600 m s^{-1} for the fractured bedrock-fresh bedrock interface.

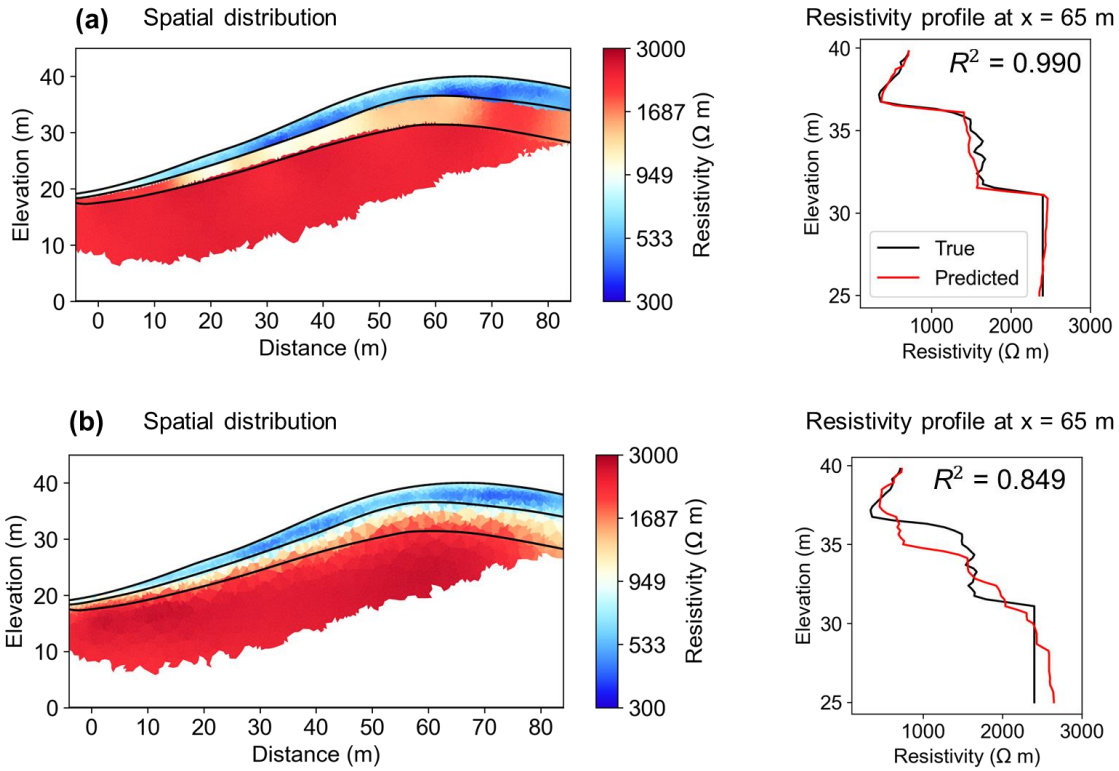

Figure 6. Reconstructed resistivity for the synthetic subsurface model: (a) new method incorporating structural information; and (b) traditional method using smoothness-based regularization.

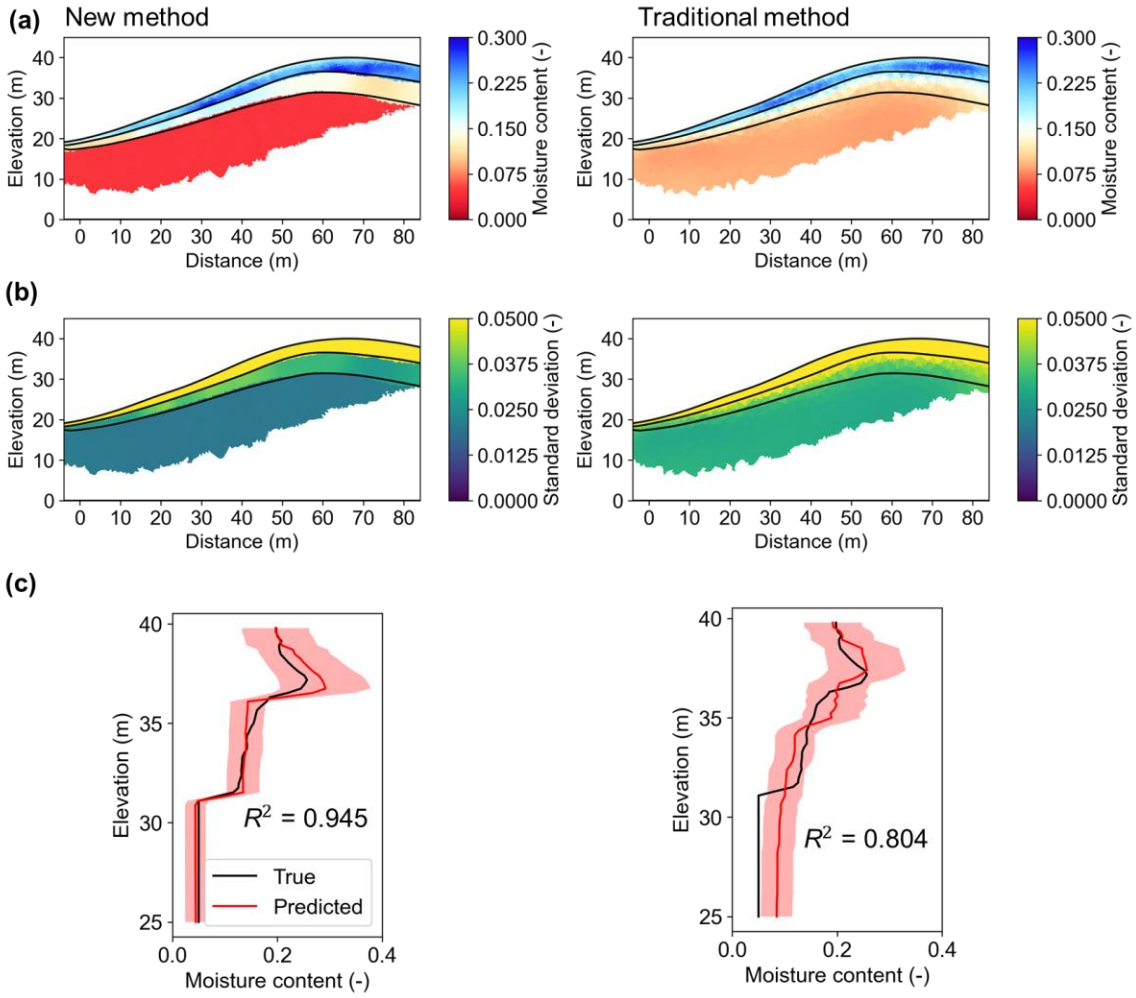

Figure 7. Comparison of the estimated moisture content of the synthetic model using new and traditional methods: (a) mean moisture content, (b) standard deviation of moisture content, and (c) mean and standard deviation of moisture content along elevation at distance x = 65 m.

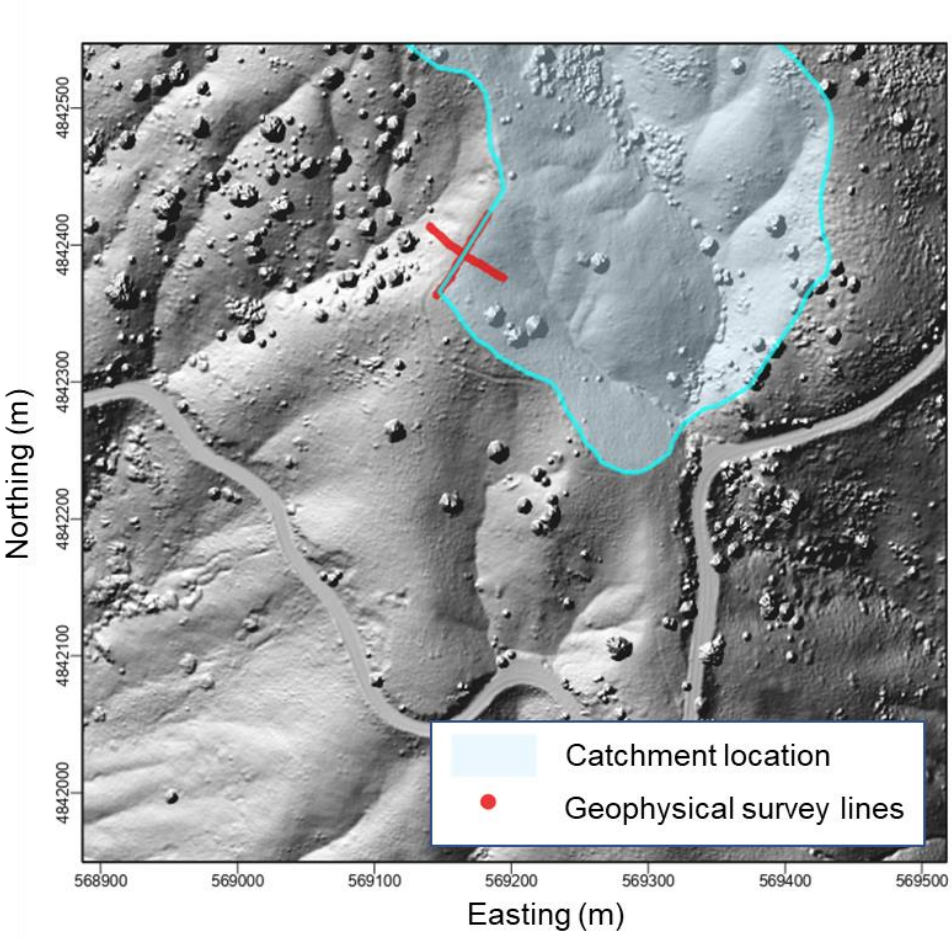

Figure 8. Map showing the location of the studied catchment and geophysical survey lines. The catchment is within the Dry Creek Experimental Watershed, Idaho (McNamara et al., 2005).

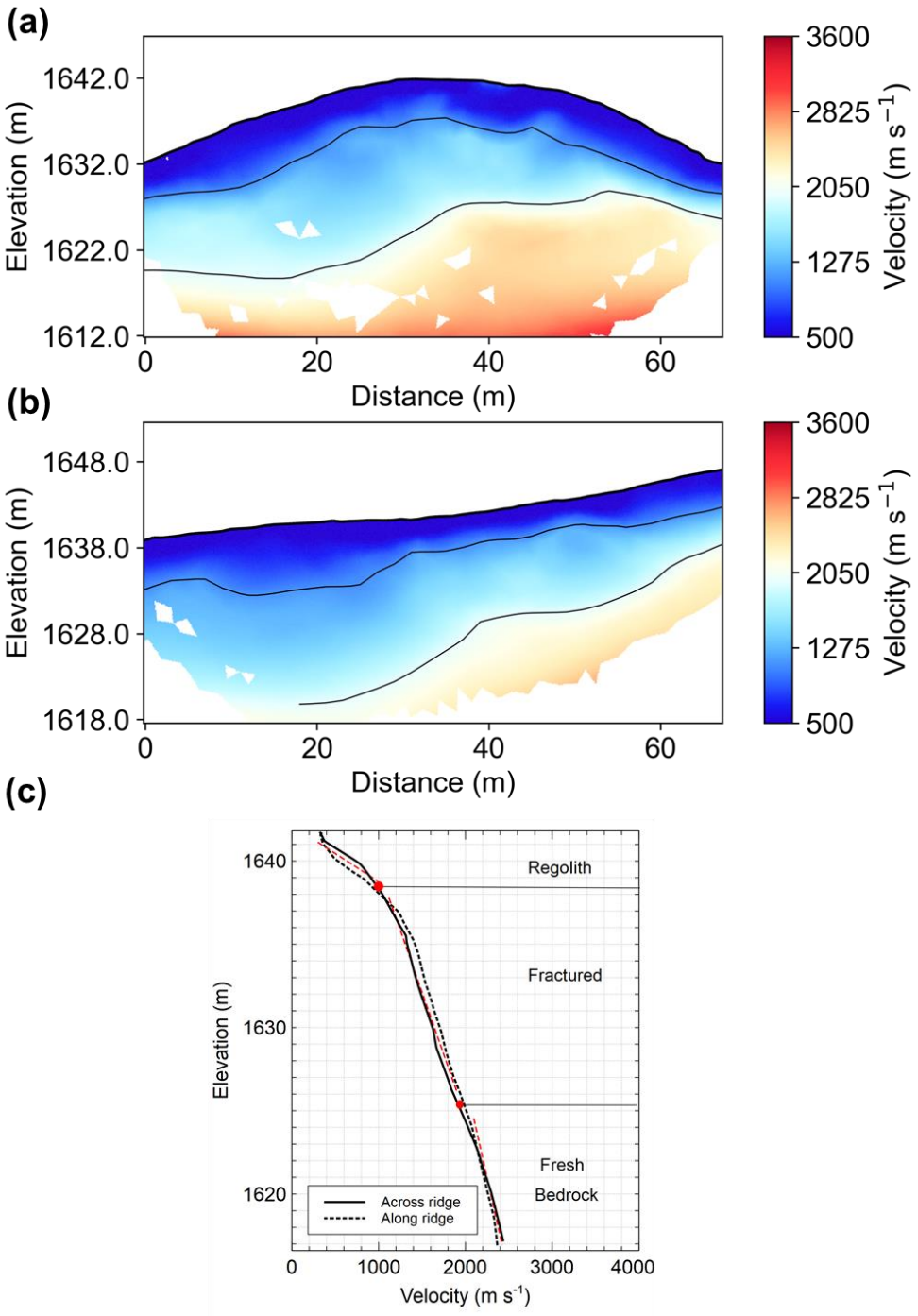

Figure 9. Reconstructed velocity distributions at the field site: (a) survey line across the ridge, (b) survey line along the ridge, and (c) velocity-elevation profiles at the intersection point of the two survey lines. In (a) and (b), solid lines indicate the inferred critical zone interfaces.

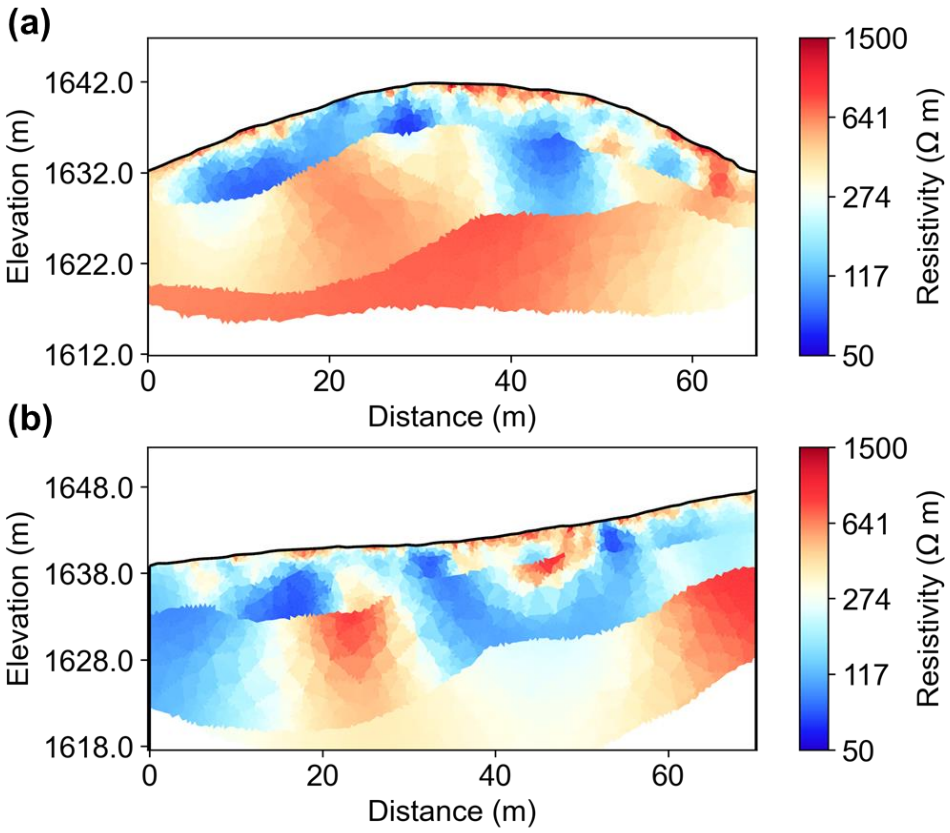

Figure 10. The reconstructed resistivity distributions of the field site using structure-constrained inversion: (a) survey line across the ridge and (b) survey line along the ridge.

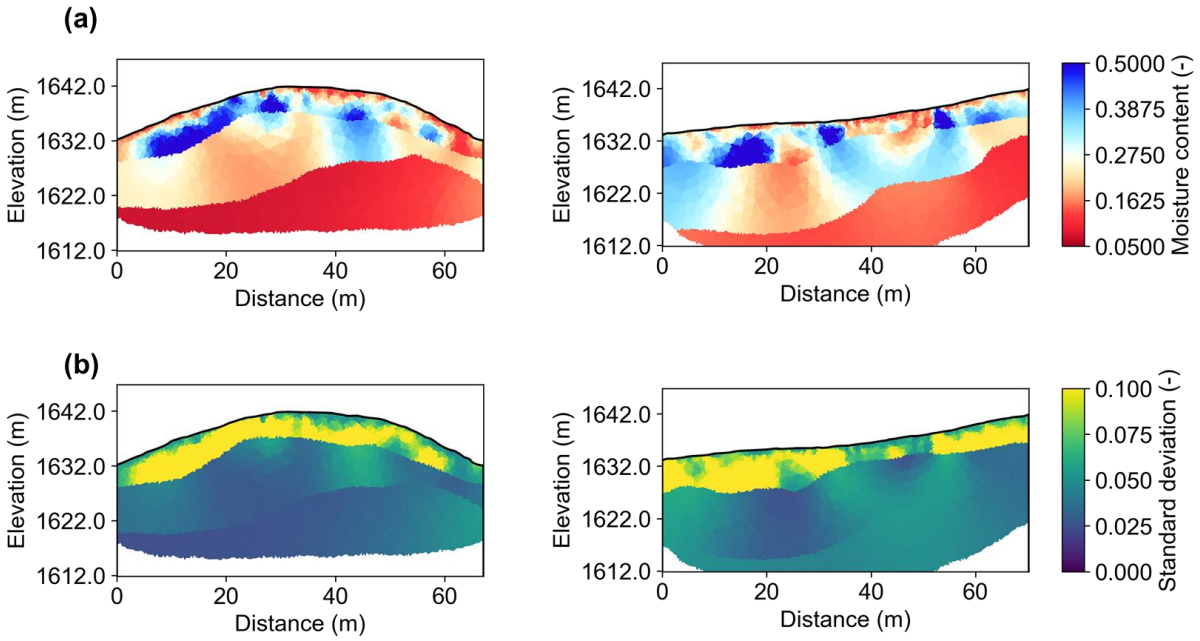

Figure 11. The moisture content results of the field site estimated from resistivity measurements: (a) mean value and (b) standard deviation.

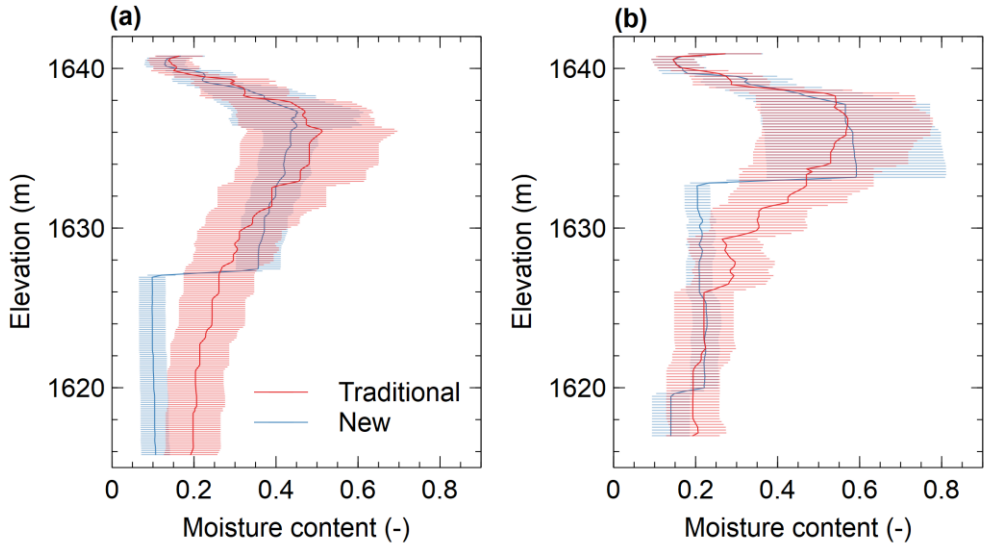

Figure 12. Comparison of the estimated moisture content–elevation profiles at the field site: (a) at distance x = 45 m on the survey line across the ridge and (b) at x = 17 m on the survey line along the ridge. The shaded area represents the uncertainty of the moisture content estimation.

Tables

Table 1. The physical properties of different structural units of the synthetic subsurface model. MC stands for Monte Carlo simulation.

Subsurface structural units		Saturated resistivity ρ_{sat} (Ω m)	Saturated resistivity related to surface conduction ρ^{s}_{sat} (Ω m)	Saturation exponent n (-)	Porosity ϕ (-)
Regolith	Mean value and variation range	170 [100,350]	510 [400,1400]	2.2	0.4 [0.25,0.5]
	Range used in MC	[80, 400]	[400,3200]	[1.8, 2.5]	[0.25, 0.5]
Fractured bedrock	Mean value and variation range	1100 [500,1920]	-	1.8	0.18 [0.11,0.25]
	Range used in MC	[600, 1200]	-	[1.6, 2.0]	[0.12, 0.25]
Fresh bedrock	True value	2400	-	2.5	0.05
	Range used in MC	[1800, 2800]	-	[2.4, 2.6]	[0.01, 0.08]

Table 2. Variation ranges of the petrophysical properties used to interpret the resistivity measurement at the field site.

Subsurface structural units	Saturated resistivity ρ_{sat} (Ω m)	Saturated resistivity related to surface conduction ρ^{s}_{sat} (Ω m)	Saturation exponent n (-)	Porosity ϕ (-)
Regolith	[50, 250]	[400,3200]	[1.3, 2.2]	[0.25, 0.5]
Fractured bedrock	[165, 350]	-	[2, 2.2]	[0.2, 0.3]
Fresh bedrock	[325, 1000]	-	2	[0.05, 0.15]